Fatigue Simulation of Human Cortical Bone using Non-Homogeneous Finite Element Models to Examine the Importance of Sizing Factors on Damage Laws

Steven Francis Ryan

Thesis submitted to the faculty of the Virginia Polytechnic Institute and State University
in partial fulfillment of the requirements for the degree of

Master of Science
In
Engineering Mechanics

John Cotton, Chair
Norman Dowling
J. Wallace Grant

May 9, 2006
Blacksburg, Virginia

Keywords: finite element modeling, bone, fatigue simulations, damage, sizing factors
non-homogeneous finite element models, stressed volume

Fatigue Simulation of Human Cortical Bone using Non-Homogeneous Finite Element Models to Examine the Importance of Sizing Factors on Damage Laws

Steven Francis Ryan

ABSTRACT

Finite element modeling has become a powerful tool in orthopedic biomechanics, allowing simulations with complex geometries. Current fatigue behavior simulations are unable to accurately predict the cycles to failure, creep, and damage or modulus loss even when applied to a bending model. It is thought that the inhomogeneity of the models may be the source of the problem. It has also been suggested that the volume size of the element will affect the fatigue behavior. This is called a stressed volume effect. In this thesis non-homogeneous finite element models were used to examine the effects of "sizing factors" on damage laws in fatigue simulations.

Non-homogeneous finite element models were created from micro computed tomography (CT) images of dumbbell shaped fatigue samples. An automatic voxel meshing technique was used which converted the CT data directly into mesh geometry and material properties.

My results showed that including these sizing factors improved the accuracy of the fatigue simulations on the non-homogeneous models. Using the Nelder-Mead optimization routine, I optimized the sizing factors for a group of 5 models. When these optimized sizing factors were applied to other models they improved the accuracy of the simulations but not as much as for the original models, but they improved the results more than with no sizing factors at all. I found that in our fatigue simulations we could

account for the effects of stressed volume and inhomogeneity by including sizing factors in the life and damaging laws.

Acknowledgements

First I would like to thank my beautiful wife Karen who has supported me every step of the way through these difficult times. Her everyday focus and courage has been my driving force and inspiration. I could not have completed this without her love and support. I also need to thank my parents who have given so much to make this possible. Without their love and encouragement this would not have been possible. I would like to thank my grandfather whose support and inspiration over the years has been never ending and invaluable. Also I need to acknowledge my grandmother whose memory drives me every day to be the best person that I can be.

I would like to express my appreciation to Dr. Cotton, my advisor and committee chairman, for his patience and support while writing this thesis. Especially during the writing process, I think he now understands why I chose to be an engineer and not an English major. I would also like to thank the Virginia Tech-Wake Forest School of Biomedical Engineering & Sciences and the Virginia Tech department of Engineering Mechanics for allowing me to take time off to recover when I was ill.

Table of Contents

List of Figures

List of Tables

Chapter 1: Introduction

The quantification of the mechanical behavior of healthy bone is a necessity for the study of implant failure, femoral neck fractures, stress fractures and senile fractures. Fatigue testing on bone can help define empirical relationships and methods that predict the mechanical behavior and properties (Cotton, Winwood et al. 2005). These methods can then simulate implants in an attempt to increase the fixation life in the surrounding bone (Taylor and Tanner 1997). Stress fractures that are common in athletes and military recruits, occur in healthy bone under high cyclic loading situations; while senile fractures occur in diseased bone (Donahue, Sharkey et al. 2000).

Numerous studies have investigated the fatigue behavior in bone (Carter and Caler 1983; Zioupos, Wang et al. 1996; Zioupos, Currey et al. 2001; Cotton, Winwood et al. 2005). These studies have examined cycles to failure vs. stress, damage vs. stress and have shown bone can experience a loss of the material stiffness, loss of strength, and accumulation of permanent strain during fatigue. Damage in bone can be defined as loss of the mechanical properties reducing the usefulness. The damaged state could be found by measuring the permanent changes in the mechanical behavior during a damaging event.

Computed tomography (CT) uses x-ray equipment to obtain cross-sectional images of the body. CT images map different attenuation coefficients, which differentiate bones, organs and other tissues. The information from a CT image can be used to model specific geometry and modulus of bone.

Finite element (FE) modeling has become a powerful tool in orthopedic biomechanics, allowing simulations with complex geometries to be solved. Advanced material behavior has been simulated including; fatigue behavior (Taylor, Verdonschot et al. 1999), implant failure (Taylor and Tanner 1997) and fracture location prediction (Keyak, Rossi et al. 2001). Even though finite element analysis is widely used, the results can vary due to meshing techniques used before solving the problem (Viceconti, Bellingeri et al. 1998).

This thesis describes the first FE simulation of fatigue behavior in non-homogeneous samples of human cortical bone. Previous fatigue behavior simulations used homogeneous FE models of human cortical bone samples. The simulation's predicted modulus degradation and permanent strain data were in close agreement with the experimental data, both in terms of the trends and absolute magnitudes (Taylor, Verdonschot et al. 1999). This simulation technique did not accurately predict the cycles to failure, creep or damage when applied to a model representing cancellous bone. It was suggested that the inhomogeneity of the model could be the source of the problems (Taylor, Cotton et al. 2002). It has also been proposed the fatigue behavior of bone like many other materials is dependent on the size of the test specimen called stressed volume or "sizing effects" (Taylor and Kuiper 2001). In our simulation non-homogeneous FE models of cortical bone samples were created using an automatic voxel meshing technique, where CT images were used as source information for the geometry and material properties. The primary goal of this thesis was to examine the effects of incorporating "sizing factors" (K_N, K_D, and K_{cr}) into the life and damaging laws to account for sizing effects and inhomogeneity to achieve improved fatigue simulations for

non-homogeneous FE models. Where, the life and damaging laws are the empirical equations from Cotton, Winwood, et al. (2005).

This chapter presents background information relevant to the of fatigue behavior simulation of cortical bone. The mechanical behavior of cortical bone during *in vitro* fatigue testing is described. FE meshing techniques, models, and simulations relevant to this research are discussed.

1.1 Bone

There are two major classifications of bone: cortical and cancellous bone. Cortical, or compact bone represents nearly 80% of the skeletal mass and forms a structural shell around most every bone in the body (Carter and Hayes 1977). It is stiff with a longitudinal elastic modulus between 14-20 GPa (Taylor, O'Reilly et al. 2003) and a low porosity of 5-30% (Carter and Hayes 1977; Cowin 2001). Cancellous, or trabecular bone, while only representing 20% of the skeletal mass represents 80% of bone volume. Cancellous bone is less dense and has a porosity ranging from 30-90% (Carter and Hayes 1977). Cancellous bone forms low weight interior scaffolding, which to helps bone maintain its shape by absorbing compress forces.

1.2 Role of Fatigue in Orthopedic Problems

Cortical bone when subjected to cyclic loading exhibits a reduction of elastic modulus, accumulation of permanent strain for non zero mean stresses, and failure at stresses below the static strength, which are all indicative of fatigue damage. Fatigue damage can contribute to femoral neck fractures (Keyak, Rossi et al. 2001), stress fractures (Valimaki, Alfthan et al. 2005) and failure of implants (Taylor and Tanner 1997).

Uniaxial Fatigue Testing

A servo-hydraulic machine is usually used to perform fatigue tests. The fatigue specimens are clamped in the grips of a testing machine equipped with a water bath chamber maintained at body temperature, 37˚C. The load and displacement are recorded with time, and the load is converted into stress σ, by dividing by the initial cross-sectional area. The engineering strain values, ε are produced from the movement of the actuator or extensometer. A machine-generated loading waveform is used to cycle specimens at a cycle frequency of 2 Hz between a near zero load level (Zioupos, Wang et al. 1996; Zioupos, Wang et al. 1996). Other examples of uniaxial fatigue testing can be seen in (Carter and Hayes 1977; Pattin, Caler et al. 1996; Lee, O'Brien et al. 2000).

Cycles to Failure

The traditional approach to studying the cycles to failure of bone usually involves the stress-life (σ-N) approach (Carter and Hayes 1977), where specimens are cycled at

various stress levels in order to determine the number of cycles to failure at a specific stress. From this data a σ-N_f diagram is made, in which the stress is plotted against the number of cycles to failure. When both values are plotted on log scales, the distribution is roughly linear and has been expressed as a power law relationship,

$$N_f = A\sigma^B \tag{1.1}$$

where A and B are constants from the data (Basquin 1910). Damage has been expressed as the remaining life of the material. In this case the damage, *d*, is thought to increase inversely proportional to the total cycles to failure, N_f,

$$d = n / N_f \tag{1.2}$$

n represents the number of cycles experienced; hence in this case damage represents a fraction of the remaining life.

Modulus degradation

Bone, when subjected to a uniaxial tensile load exhibits microscopic losses in continuity leading to microcracks which decrease the longitudinal stiffness. The damage can be interpreted as the ratio of the damaged area, which no longer carries the load to the total load, or as the remaining life of the material (Kachanov 1986). When observing damage as a functional loss of stiffness it can be expressed as,

$$d = 1 - E_i / E_o \tag{1.3}$$

where, in fatigue studies, E_i, is the current secant modulus (Zioupos, Wang et al. 1996). The undamaged modulus, E_o, can be defined as the initial tangent modulus of the first load cycle (Zioupos, Currey et al. 1994; Courtney, Hayes et al. 1996).

Loss of Strength

Strength degradation is thought to have more clinical importance as a damage state measure than stiffness, but characterizing strength degradation is difficult because there is no easy way to define an undamaged strength value. It would be necessary to destroy the samples to compare the failure event across a population to evaluate the change in strength (Cowin 2001).

Cracking

It has been shown that during *in vitro* fatigue testing, fractures of machined bone specimens are the result of a progressive accumulation of micro damage and micro cracks that form ahead of catastrophic macrocracks. This microdamage contributes to the formation of stress fractures and fragility fractures (Schaffler et al. 1995). The resistance of any material to fatigue failure is a function of its resistance to either the initiation or propagation of cracks, or both.

Creep

Bone, like many other engineering materials, exhibits a three stage creep (Figure 1.1) (Carter and Caler 1983). The primary stage is a rapid concave-down curve followed by a slower, constant rate, called the second stage; and then a rapid concave-up curve, called the third stage. The degree of modulus degradation and permanent strain, ε_{pn} accumulation has been shown to be dependent on the magnitude and sign of the applied stress or strain. It has been shown for a zero to tensile (0- T) cyclic load test that the

permanent strain fits the functional form and magnitude of creep, which can be seen in (Cotton, Zioupos et al. 2003). Figure 1.2 from Cotton, Zioupos et al. (2003) shows the accumulation of percent permanent strain vs. the number of cycles from 53-year-old female fatigue sample with an applied normalized stress of 0.0049 (4900 με). The curve contains the three portions that are typical to the functional form of creep.

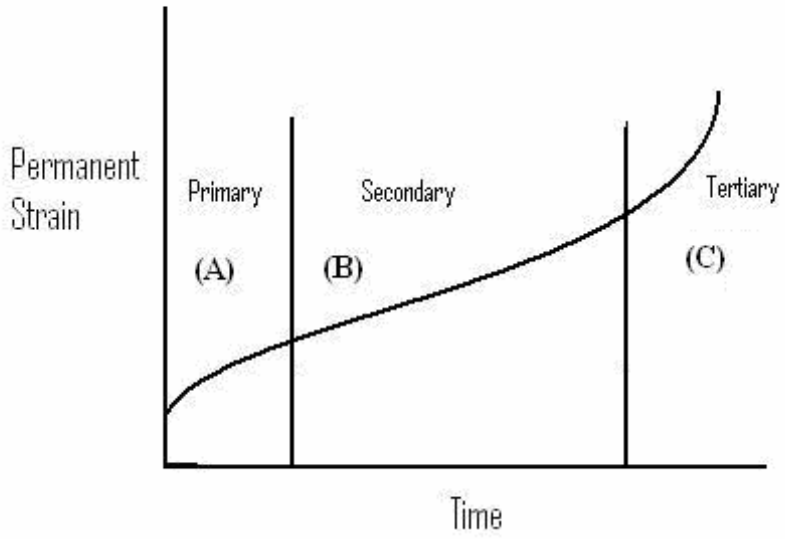

Figure 1.1: Basic functional form of creep: (A) Primary stage, rapid concave-down section, (B)Secondary stage, slower almost constant rate, (C) Third Stage, rapid concave-up before failure.

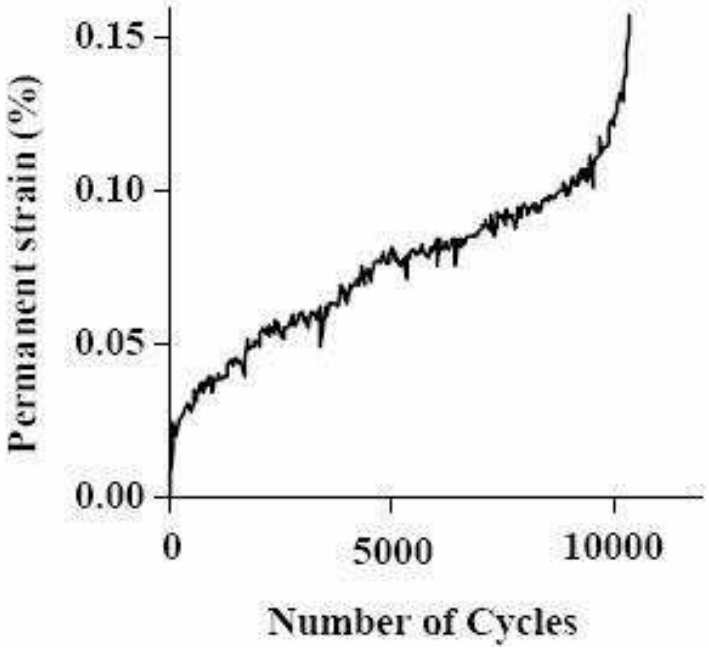

Figure 1.2: Accumulation of percent permanent strain plotted against the number of cycles from a 53-year-old female fatigue sample with an applied normalized stress of 0.0049 με; the curve contains the typical form of creep (Cotton, Zioupos et al. 2003).

1.3 Finite Element Analysis in Orthopedics

FE models allow the complex geometries and properties of bone to be represented. FE modeling of bone provides a valuable tool for examining behavior. FE models can be created by transforming a CT image into a solid model and then meshing the solid model, and then material properties are applied from the CT image. FE models can also be produced by direct or automatic meshing, where the geometry and material properties are taken directly from the CT image.

Computed Tomography Images

Computed tomography describes a procedure in which x-ray measurements are made at multiple angles around an object and are then used to reconstruct a section, or slice, of the object. Each local volume of interest, the size of which depends on scanner resolution, is called a voxel. The CT numbers measured for a voxel are related to the x-ray attenuation coefficient of the material in that volume. This allows differentiation between materials with different attenuation coefficients. CT images can provide accurate information on bone geometry since the attenuation coefficient of bone tissue is much higher than the one of the surrounding soft tissues which results in contrasting edges. It has also been shown that the numbers in the CT images can be related with the mechanical properties of bone tissues (Carter and Hayes 1977; Taddei, Pancanti et al. 2004). A three-dimensional scan is formed by combining multiple adjacent slices. The CT image is essentially a three-dimensional array in which CT numbers are stored (Goodenough 2000).

Finite Element Meshes Created From Solid Models

Once a solid model has been created from CT data there are various methods for creating FE meshes using various commercial FE software packages. A more detailed description and comparison of three techniques and the software used to perform the meshing can be found in Viceconti, Bellingeri et al. (1998). FE meshes created from solid models produce smooth surface geometries.

Finite Element Meshes Created directly from CT images

Keyak, Meagher et al. 1990 developed a method that converts voxel information obtained from CT images directly into elements. The apparent material density, ρ which is dominated by the mineral content, is calculated through a linear relationship (McBroom, Hayes et al. 1985). Bone mineral content shows up well in CT images because of the high attenuation coefficients (Taddei, Pancanti et al. 2004). The elastic modulus for each voxel is then be calculated by using a power-law relationship such as,

$$E_o = A\rho^B \text{ MPa} \tag{1.4}$$

where A and B are experimentally derived constants. This equation can be rewritten as,

$$\log E_o = \log \mathrm{A} + \mathrm{B} \log \rho \tag{1.5}$$

the relationship between E_o and ρ is linear when plotted on log-log scale. The regression slope for the data is B and the intercept is log A (Carter and Hayes 1977).

This method uses a simplified element structure, a regular eight-node brick, to define the model. The geometry is created by stacking the contours of each layer of the CT scan. These brick elements do not accurately model the surface geometry of the bone surface. The accuracy of the bone geometry can be increased by reducing the size of the elements (Keyak, Meagher et al. 1990; Keyak, Fourkas et al. 1993). Figure 1.3 shows a mesh created from a solid model and a mesh by an automatic voxel technique, as described by the above procedure. The meshes in Figure 1.3 were created using the same geometry (Viceconti, Bellingeri et al. 1998).

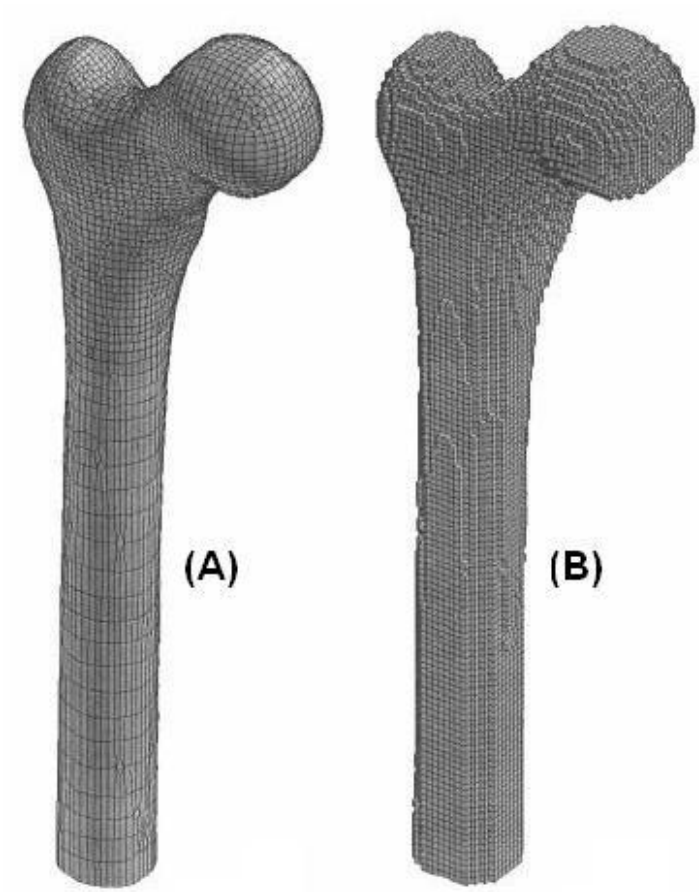

Figure 1.3: Comparison of FE meshes of femur: (A) Mesh created from solid model, (B) Mesh created from automatic voxel meshing method (Viceconti, Bellingeri et al. 1998).

1.4 Numerical Models

Taylor, Verdonschot et al. (1999) developed a technique to simulate the tensile fatigue behavior of human cortical bone samples. In their study they assumed damage, *d*, to be: (i) a linear function of the life fraction $d = n / N_f$; (ii) zero at the beginning of the analysis rising to a value of 1 at failure. The number of load cycles to failure, N_f at a given stress level was determined using a power law,

$$Log(N_f) = -28.23 \log(\sigma / E_0) - 58.43 \qquad (1.6)$$

where E_0 is the initial Young's modulus of the specimen and σ is the applied tensile stress. During Fatigue the current modulus, E_i and permanent strain, ε_{pn} were assumed to be non-linear functions of the damage and were chosen to match experimental fatigue data.

$$E_i = a(d)^3 + b(d)^2 + c(d) + E_0 \tag{1.7}$$

$$\varepsilon_{pn} = e(d)^f \tag{1.8}$$

where *a*, *b*, *c*, *e*, and *f* are material dependent, linear functions of the normalized stress level.

$$a = 2.346(\sigma / E_o) - 19032 \tag{1.9}$$

$$b = -2.567(\sigma / E_o) + 21737 \tag{1.10}$$

$$c = -1.425(\sigma / E_o) + 4320 \tag{1.11}$$

$$e = 0.931(\sigma / E_o) - 3395 \tag{1.12}$$

$$f = 1.52\text{x}10^{-4}(\sigma / E_o) - 0.525 \tag{1.13}$$

where all fatigue data was taken from Zioupos, Wang et al. (1996).

Cotton, Winwood et al. (2005) relate the cycles to failure N_f, damage rate $\Delta d/\Delta n$ and creep rate $\Delta\varepsilon_{cr}/\Delta n$ to the normalized stress range σ/E^*, where σ is the applied stress, during a zero-tension (0-T) fatigue test.

The damage in the *i*th cycle, d_i was defined as the fraction loss in the modulus and was expressed as,

$$d_i = 1 - E_i / E_o \tag{1.14}$$

where E_0 is the initial modulus. A regression analysis was performed for damage from 10% to 90% of the sample life against the cycle number. During this portion of the life

the damage tends to be linear and the slope of the regression line represents the damage rate per cycle.

The creep per cycle was calculated using the same method. It was found that the cycles to failure, N_f creep rate, $\Delta\varepsilon_{cr}/\Delta n$ and damage rate $\Delta d/\Delta n$ could be expressed as a function of the normalized stress (Cotton, Winwood et al. 2005),

$$N_f = A_f\left(\frac{\sigma}{E^*}\right)^{B_f}, \qquad \text{Log } A_f\text{=-27.9 } B_f\text{=-13.5} \tag{1.15}$$

$$\frac{\Delta\varepsilon_{cr}}{\Delta n} = A_{cr}\left(\frac{\sigma}{E^*}\right)^{B_{cr}}, \quad \text{Log } A_{cr}\text{=33.9 } B_{cr}\text{=17.1} \tag{1.16}$$

$$\frac{\Delta d}{\Delta n} = A_d\left(\frac{\sigma}{E^*}\right)^{B_d}, \qquad \text{Log } A_d\text{=35.5 } B_d\text{=17.0} \tag{1.17}$$

1.5 Simulating Fatigue using FEA

Taylor M., Verdonschot et al. (1999) simulated the tensile fatigue behavior of homogeneous human cortical bone samples by implementing their above numerical model with FE analysis.

At the beginning of each iteration the FE model was loaded and the stresses within each element calculated. The number of remaining cycles to failure, n_r for each element was calculated using,

$$\mathrm{n_r} = \mathrm{N_f}\left(1-\mathrm{d}\right) \tag{1.18}$$

where N_f is calculated from Equation 1.6. The element with the lowest number of cycles to failure remaining within the model was then determined. To simulate damage and creep an iterative solution was implemented. An iteration can represent 1 to tens of thousands loading cycles. The number of loading cycles, Δn, for the current iteration was based on a chosen percentage of the lowest cycles to failure within the model. The

change in damage, Δd, within each element was calculated and added to the total damage, d. If the damage of an element reached a value of 1, the element was removed causing the load to be redistributed to surrounding elements. The modulus loss was calculated using Equation 1.7, and permanent strain using Equations 1.8, 1.12, 1.13. At the start of the next iteration the material properties for each element were updated and this procedure was repeated until failure of the sample occurred.

This approach was used to predict the cycles to failure, modulus degradation and the permanent strain. The corresponding FE models were assumed isotropic, homogeneous and linear elastic with only one quarter of the specimen being modeled due to symmetry. Simulations of eight cortical bone samples were run and compared to the experimental data from Zioupos, Wang, et al. (1996). They found that the results of the FEA simulations were in close agreement with the experimental data (Taylor, Verdonschot et al. 1999).

1.6 Stressed Volume

Taylor, D. and Kuiper (2001) proposed the fatigue behavior of bone like many other materials is dependent on the size of the test specimen used. It is known that larger components will tend to fail more easily by fatigue than small components subjected to the same stress levels due to a weakest-link phenomenon: where weak regions exist from pre existing micro cracks. The life of a given specimen is controlled by the properties of the weakest region. This causes shorter lives for larger components since a large stressed volume has a higher probability of containing a weak region. This also causes scatter in

the lives of components of the same size (Taylor and Kuiper 2001). The number of cycles to failure, N_f, is described as,

$$N_f = A\Delta\sigma^B \tag{1.19}$$

Taylor, D. and Kuiper (2001) showed the fatigue strength of bone is affected by the sample volume and that larger bone samples tend to have lower fatigue strengths. The number of cycles to failure for specimens of different volumes can be predicted using,

$$\frac{\Delta\sigma_o}{\Delta\sigma^*} = \left(\left(\frac{-V_{so}}{V_s + \mathrm{V}^*}\right) \ln\left(0.5\right)\right)^{\frac{1}{\mathrm{B}}} = K_n \tag{1.20}$$

where V_s is the stressed volume and V_{so} the original specimen volume. V^* is a constant added to compensate for microstructures or for stressed volumes below 10 mm^3. B and $\Delta\sigma^*$ are constants that express the degree of scatter in the data.

1.7 Summary of Research Conducted in this Thesis

FE meshes of human cortical bone fatigue samples were created through an automated voxel meshing technique in order to determine to the effects of adding "sizing factors"; K_N, K_D, and K_{cr} to fatigue simulations. I took the existing simulation from Taylor M., Verdonschot et al. (1999) and added the sizing factors to the life, damage and creep laws, which are empirical equations (Equations 1.15-1.17) from Cotton, Winwood, et al. (2005).

Micro CT images of ten dumbbell fatigue samples were used as source data to derive the geometry and non-homogeneous material properties for each FE mesh. The micro CT images were randomly divided into two groups; "Sample group 1" (SMP1 or

optimization) and "Sample group 2" (SMP2 validation). The automatic meshing technique produced a mesh size of 0.28 mm face length for every cubic element for both sample groups, which would be used for the majority of the analysis performed. Additional mesh sizes of 0.21 and 0.14 mm were produced for the SMP1 group these meshes will be used to check the effects of mesh size on model properties and the fatigue simulations. The meshes were imported into MSC MARC (MSC software, Santa Ana, CA) to create FE models. Boundary conditions and loads were applied to simulate *in vitro* fatigue testing conditions.

The SMP1 group was used to determine optimal sizing factors for each FE model in the group using the Nelder-Mead optimization. FEA simulations would then be compared with 1) predicted values of the fatigue behavior computed from Equations 1.15-1.17, 2) FEA simulations of the current stressed volume approach which only includes the K_N and 3) the previous method which does not include any sizing factors. The accuracy of the results were computed using an average percent error between the FEA simulations and the empirically predicted values for the cycles to failure, N_f damage rate, $\Delta d/\Delta n$ and creep rate, $\Delta \varepsilon_{cr}/\Delta n$. The SMP2 group was used to evaluate the success of the sizing factors on other models. FEA simulations were run at a different mesh size to examine the effects of different mesh size on our determined values.

Chapter 2: Materials and Methods

In this chapter, the materials and methods used in the finite element simulation of the fatigue behavior- cycles to failure, damage per cycle and creep per cycle are described. The CT images used as data sources are presented in Section 2.1. Section 2.2 describes the processes used to develop the models used in the simulations. The method of simulating the fatigue behavior is shown in Section 2.3. Descriptions of the analyses performed can be found in Section 2.4.

2.1 CT Images

CT images for ten fatigue samples originated from the Department of Oral Growth & Development, Queen Mary, and University of London. The dumbbell shaped cortical bone samples were machined at Crainfield University,Shrivenham,UK from the femur of a 74 year old female cadaver. All were longitudinally oriented; with a cross section of approximately 5.3 mm^2 and a gauge length of 10 mm. The scans had a resolution of 14.95 μm and the image sizes varied depending on the sample and are shown in Table 2.1.

The CT images were randomly divided into two groups (Table 2.2), "Sample group 1" (SMP1) group and a "Sample group 2" (SMP2) group. The SMP1 group was used to determine the optimal sizing factors implemented in the simulations to increase accuracy of fatigue on each individual model. The SMP2 group was used to check the effectiveness of the sizing factors found on other models. Table 2.2

Table 2.1: Micro CT image data

	x	*y*	*z*	File size
CT name	Voxels	Voxels	Voxels	MB
Pz1tm	380	240	912	83.17
Pz2tm	420	320	912	122.57
Pz3tm	370	370	912	124.85
Pz4tm	370	370	912	124.85
Pz5tm	280	400	912	102.14
Pz6tm	300	380	912	103.97
Pz7tm	240	400	912	87.55
Pz8tm	440	240	912	96.31
Pz9tm	360	260	912	85.36
Pz10tm	420	390	912	149.39

Table 2.2: CT images randomly divided into groups

"Sample group 1" (SMP1)		"Sample group 2" (SMP2)	
CT name	Model name	CT name	Model name
Pz1tm	SMP1-1	Pz2tm	SMP2-1
Pz3tm	SMP1-2	Pz4tm	SMP2-2
Pz5tm	SMP1-3	Pz7tm	SMP2-3
Pz6tm	SMP1-4	Pz9tm	SMP2-4
Pz8tm	SMP1-5	Pz10tm	SMP2-5

2.2 Model Development

Finite element models of the human cortical bone fatigue samples were created using the CT images as source information. The process of converting a CT image into a finite element model required: 1) image processing, 2) creating meshes through an automatic voxel technique and 3) applying loads and boundary conditions. Figure 2.1 shows an outline of the modeling process used to create the finite element models.

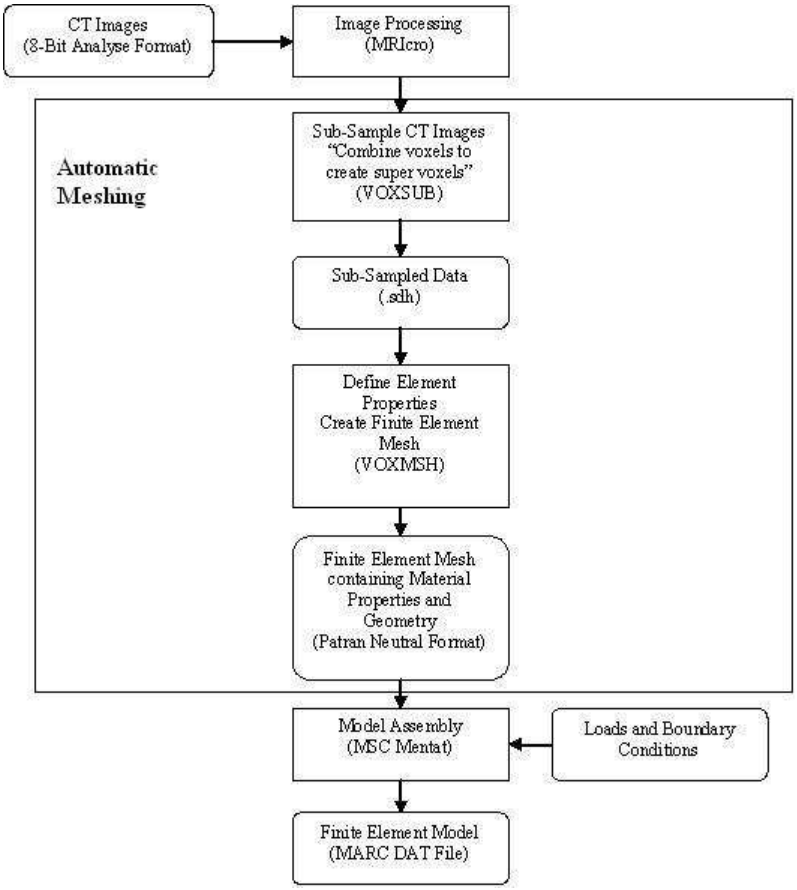

Figure 2.1: Modeling process. Inputs and outputs are shown in rounded boxes with the corresponding file types if applicable. Major steps are shown in boxes with the software used

Image Processing

The first step in creating the meshes was rotating the CT images in MRIcro (Chris Rorden, University of South Carolina, Columbia, SC). The rotations were performed to simplify the surface geometry of the models once the meshes were created and imported into MARC. The CT images were rotated to get the longitudinal axis of the CT images vertical; which represents the z-axis in MARC. Rotations were also performed to align

with the front and side of the samples with the x-z and y-z plane in MARC. A 3-D rendering of the desired orientation for the samples is shown in Figure 2.2. Figure 2.3 shows sample xPz3tm before and after rotations have been performed. Once the CT images were rotated the meshes could be created.

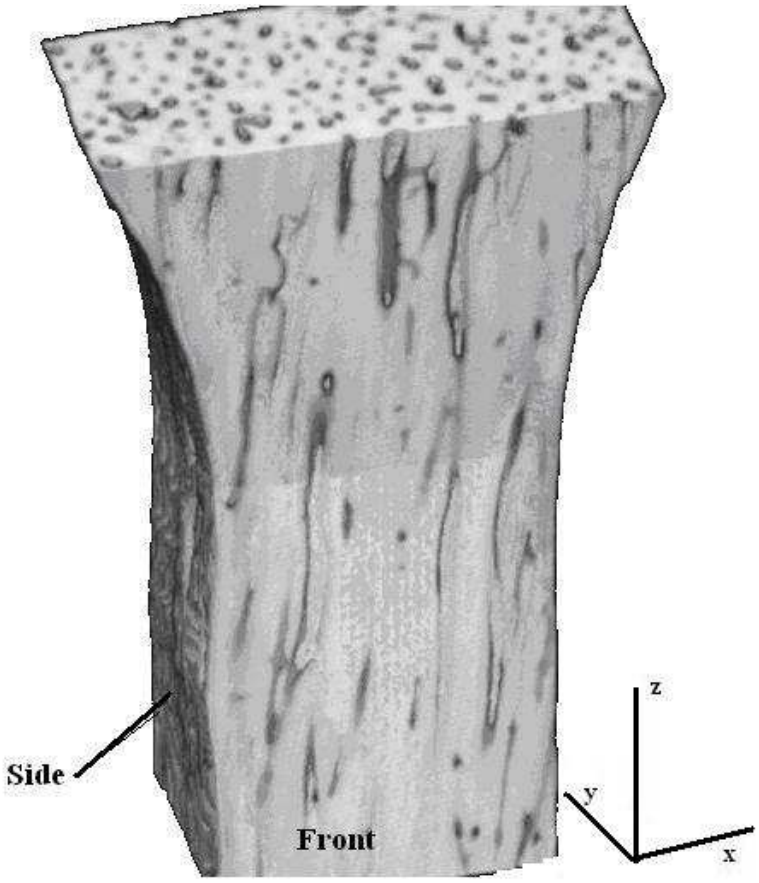

Figure 2.2: 3-D rendering of a SMP1-1: Showing desired orientation before automatic meshing to simplify surface geometry.

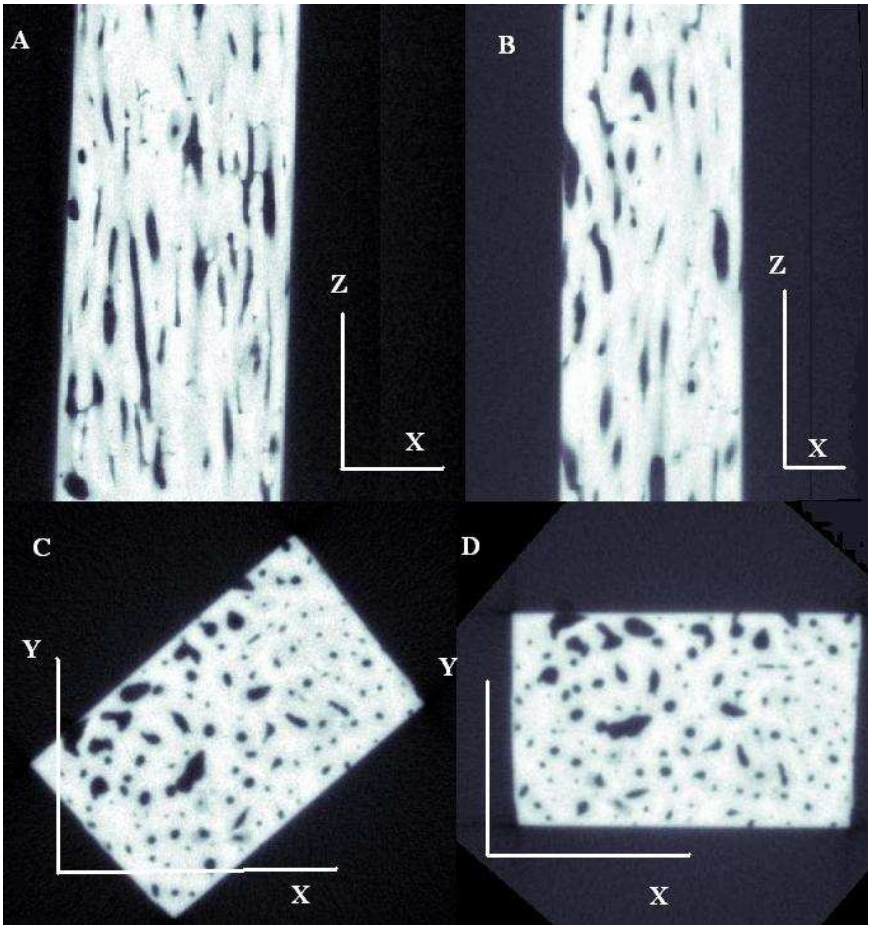

Figure 2.3: Images of Sample xPz3tm before and after rotations; (A) Longitudinal view before rotation, (B) Longitudinal view after 2 degree rotation about y-axis to get the axis vertical, (C) X-Y plane before rotation, (D) X-Y plane after 41degree rotation about z-axis

Automatic Meshing

The FE meshes were constructed using a voxel based automatic meshing technique similar to the procedure described by Keyak et al, (1990). The FE meshes were generated using two programs, VOXSUB and VOXMSH (Laboratorio di Tecnologia Medica of Istituti Ortopedici Rizzoli, Bologna – Italy). The first program VOXSUB takes the CT data and creates a sub-sampled dataset by combing voxels. The user defines input such as the number of voxels that will be combined in *x*, *y* and *z*-direction. For example if the user defined input is set to two in each direction then two

voxels each in the *x*, *y* and *z*-direction will be combined forming a larger "super voxel" now containing eight voxels. This sub-sampling generates a set of super voxels. Each super voxel is then assigned a CT number obtained as an average of the composing voxels CT number.

The user defined input was set to combine 20 voxels in each of the three orthogonal directions giving an element edge length of 0.28 mm which I will call our "normal" mesh for both the SMP1 group and the SMP2 group. This normal mesh would be used in most of the analysis performed. To test the effects of the mesh size on a model's modulus, surface geometry and fatigue behavior simulation two more meshes were created for the SMP1 group. To create these additional meshes the user defined inputs were set to 15 and 10 creating edge lengths of 0.21 (fine) and 0.14 (super fine) mm respectively.

The second program VOXMSH converts the averaged CT number for each super voxel into the tissue apparent density, ρ, using the relationship,

$$\rho = \frac{\text{brightness}}{\kappa} 1.037 \quad \text{g/cm}^3 \tag{2.1}$$

where the brightness ranged from 0-255 and κ, a scale factor determined from the calibration of the scanner. The scale factors are shown below for each sample in Table 2.3.

Table 2.3: Scale factors for CT images

CT Image	xPz1tm	xPz2tm	xPz3tm	xPz4tm	xPz5tm	xPz6tm	xPz7tm	xPz8tm	xPz9tm	xPz10tm
κ	130	130	120	130	130	120	75	130	130	130

The modulus for each super-voxel was then calculated using an empirical relationship from Carter and Hayes (1977),

$$E_o = 3790\rho^3 \text{ MPa} \tag{2.2}$$

this relationship was determined from compression data and assumed valid for tensile modulus (Keyak, Meagher et al. 1990). We used this relationship because it placed the modulus values of the models inside the reported values of cortical bone 14-20 GPa (Taylor, O'Reilly et al. 2003).

Once the material properties were assigned the super-voxels were converted into linear, isotropic, regular 8-node finite element bricks. An element and its nodes were created only if the modulus was above 1000 MPa. Those elements whose modulus was lower than 1000 MPa were ignored. The FE mesh was then created by placing nodes in a cube lattice, represented by a three dimensional array in the software. This process was repeated until all the elements and their properties for the model are created and stored in a neutral PATRAN (MSC software, Santa Ana, CA) format.

Loads and Boundary Conditions

The PATRAN files of each mesh were imported into MARC where the boundary conditions and loads were applied. Boundary conditions were applied to the bottom of the model to simulate a real test where the sample would be clamped lower than the model; this allowed movement in the transverse planes. The bottom of each model was fixed in place by first setting the nodal displacements to zero in the *z*-direction. Then the nodal displacement for the center node on the bottom of the model, point A in Figure 2.4, was

fixed in all directions. Next the *x*-displacements were set to zero for the nodes on line BC in Figure 2.4. Finally the *y*-displacements were set to zero for the nodes on line DE in Figure 2.4. This keeps the model from sliding in the axial plane.

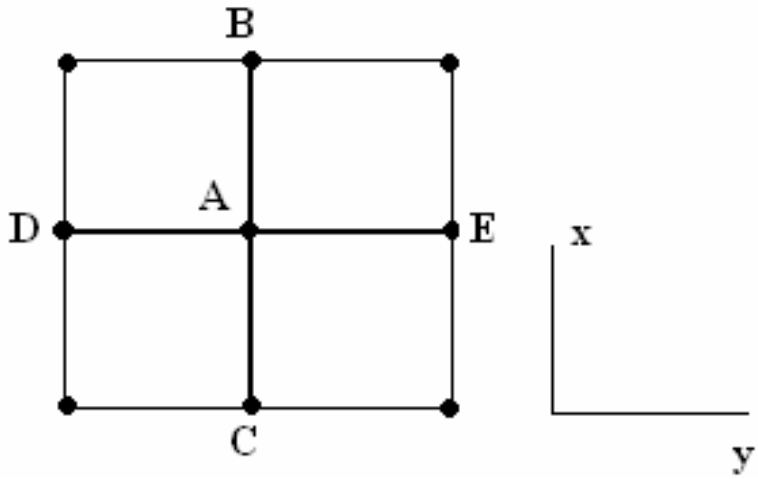

Figure 2.4: Diagram of nodal constraints for bottom of finite element models to emulate *in vitro* fatigue testing

The loading force was applied to each model to approximate an actual test where the sample is loaded above the finite element model. This was achieved by placing a point load at the center node of the top of each sample and then "tying" the remaining nodes on the top center node. "Tying" in MARC applies identical displacements for all tied nodes. In this case the nodes were tied in the *z*-direction and left free to move independently in the *x* and *y*- directions.

2.3 Simulating Fatigue Behavior

To fatigue the samples, a cyclic load was implemented within MARC where an iteration consisted of three "steps." Each step represents an increment within MARC. During the first step, "load", the force or load is applied, the load is then held during the second step, "hold", allowing creep to occur; finally during the third step, "unload" the load is removed. The loading steps for a cycle are shown in Figure 2.5. In reality steps one and two would occur simultaneous but are dived into two separate parts for computational ease. Each iteration may represent more than one cycle depending on the damage (refer to Taylor M., Verdonschot, et al. 1999).

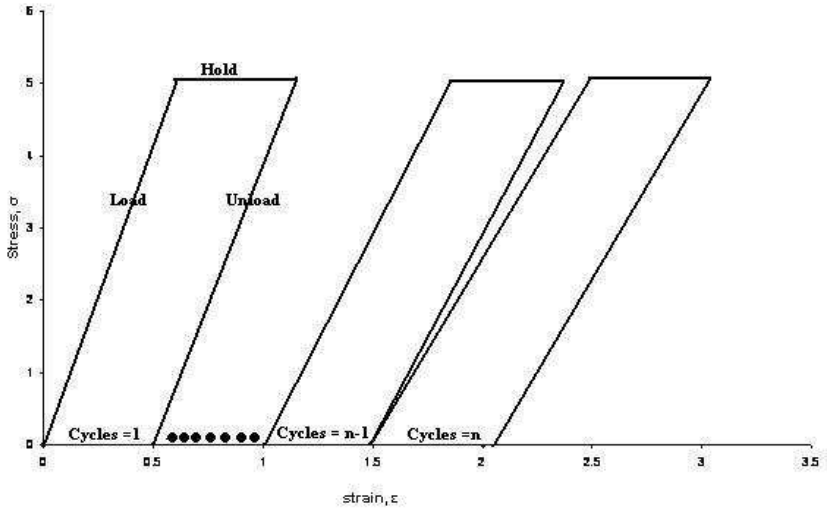

Figure 2.5: The three loading steps during an iteration; load, hold and unload

The fatigue behavior was simulated within MARC using a set of user subroutines written in FORTRAN by Taylor M., Verdonschot, et al. (1999) and later updated by

Taylor M., et al. (2002). MARC input files containg the model geometry; material properties, boundary conditions and loading conditions was also used.

The user subroutine HOOKLW is called at the beginning of every load step and sets the modulus, $E_i(k)$ for every element, where i represents the current iteration. The index k represents both the integration point and the element number, because I used a reduced integration element with one integration point per element. During the first increment each element's modulus is set to the initial modulus, $E_o(k)$. These are the moduli that were computed from the CT data and stored in the MARC input file. The damage, d (k), is set to zero because no loading or damage has occurred yet, and we assume no initial damage. The damage during a loading cycle will be computed later in the program and used to compute and update the modulus.

Next the user subroutine ELEVAR is called. This user subroutine first finds the absolute maximum value of the three principal stress values, $\sigma(k)_{prin}$ using the utility routine PRINCV within MARC for each element. Once the maximum principle stress is found for each element it is then normalized using the initial modulus,

$$\bar{\sigma}(k) = \frac{\sigma(k)_{prin}}{E_o(k)} \tag{2.3}$$

Once the normalized stress is calculated the cycles to failure for each element can be calculated using,

$$N_f(k) = \mathrm{A_f}\left(\frac{\bar{\sigma}(k)}{K_N}\right)^{\mathrm{B_f}} \tag{2.4}$$

where K_N is the "life sizing factor" added to account for sizing effects and inhomogeneity and A_f = log -27.9 and B_f = -13.3 from Cotton, Winwood et al. (2005). The minimum number of cycles to failure, $(N_f)_{\min}$ within the whole model is then found based on a

predetermined percentage of the lowest number of cycles. A more detailed explanation can be found in Taylor M., Verdonschot, et al. (1999).

Next the total number cycles run, n_i, and damage, d_i, were calculated using the subroutine UPDATVAR. The number of cycles for the current increment, Δn, were calculated based on the minimum number of cycles to failure, where Δn is the maximum of $\left(N_f\right)_{\min}$ or one. Then the total number cycles run updated is using,

$$n_i = n_{i-1} + \Delta n \tag{2.5}$$

The increase in damage for each element was calculated using,

$$\Delta d(k) = \Delta n * A_D \left(\frac{\bar{\sigma}(k)}{K_D} \right)^{B_D} \tag{2.6}$$

where A_D = log 35.5and B_D = 17.0 are from Cotton, Winwood et al. (2005) and K_D is the "damaging sizing factor." The damage is updated using,

$$d_i(k) = d_{i-1}(k) + \Delta d(k) \tag{2.7}$$

The creep for each integration point was then calculated with the user subroutine CRPLAW. The change in creep for the iteration, $\Delta\varepsilon_{cr}$, and the total creep, $\varepsilon_{cr,}$ for each element was found using,

$$\Delta\varepsilon_{cr}(k) = A_{cr} \left(\frac{\bar{\sigma}(k)}{K_{cr}} \right)^{B_{cr}} \Delta n \tag{2.8}$$

$$\varepsilon_{cr}(k)_i = \varepsilon_{cr}(k)_{i-1} + \Delta\varepsilon_{cr}(k) \tag{2.9}$$

where A_{cr} = log 33.9 and B_{cr} = 17.1 from Cotton, Winwood et al. (2005) and K_{cr} is the "creep sizing factor."

Once the creep was calculated the load was released during the third loading increment. At the beginning of the next iteration before the load was applied HOOKLAW was called again to update the modulus and damage for every element, where the new modulus is defined as,

$$E_i(k) = (1 - d_i(k))E_o(k) \tag{2.10}$$

The damage within each element was checked to see if the damage exceeded a value of 1. If an element had reached or exceeded a value of 1 then the corresponding elements modulus was reduced to 10 MPa. This essentially removes the element from the analysis which caused the stresses to be redistributed to other surrounding elements. The procedure was repeated until the sample failed. A detailed description of the simulation can be found in Taylor M., Verdonschot, et al. (1999).

2.4 Analysis Performed

Computing the Model's Initial Modulus

The initial modulus, E_o for a sample will be different from the individual moduli of the elements. The initial modulus, E_o represents the modulus for the whole model. The initial modulus, E_o for all models was computed by applying a 420 N force, F to the models and running the fatigue simulation through at least one iteration, where an iteration consists of the load, hold and unload step. In an actual fatigue test multiple cycles would be run with a small load so no damage would occur and the initial modulus

would be calculated from this data. Once the load was applied the elastic strain, ε was found using,

$$\varepsilon = \left(dz_{load} - dz_{unload}\right) \Big/ gl \tag{2.11}$$

where dz_{load} and dz_{unload} are displacements averaged from eight nodes at the top of the gage length, *gl* taken from the end of the load and unload steps respectively. The normal and super fine models had a gauge length of 9.8 mm and the fine models had a gauge length of 9.87 mm. The model's initial modulus, was the found using Hooke's Law,

$$E_o = \frac{F}{A\varepsilon} \tag{2.12}$$

where the cross sectional area, *A* of the sample and was taken from the CT image by averaging the area at slices 256, 456 and 656.

Calculating Damage and Creep Rates

The predicted fatigue behavior was computed using the empirical equations (Equations 1.15-1.17) Cotton, Winwood, et al. (2005). The simulated life, $\left(N_f\right)_{sim}$ damage, damage rate, $\left(\Delta d/\Delta n\right)_{sim}$ and creep rate $\left(\Delta\varepsilon_{cr}/\Delta n\right)_{sim}$ were calculated from the FE analysis. The displacements at the unload step could be used to calculate the permanent strain/creep in the model using,

$$\varepsilon_{cr} = \left(dz_{unload}\right) \Big/ gl \tag{2.13}$$

Then the creep per cycle can be found by dividing by the number of total cycles that occurred during the cycle. The damage rate is found by first calculating the elastic strain

for the current cycle, using Equation 2.11. Then the current modulus for the cycle and is calculated using,

$$E_i = \frac{F}{A\varepsilon} \tag{2.14}$$

The damage was then calculated using,

$$d_i = 1 - E_i / E_o \tag{2.15}$$

The damage rate was then calculated by dividing the damage by the number of cycles run.

Nelder-Mead Numerical Optimization to find K_N, K_D, and K_{cr}

I needed a direct search method to optimize a set of parameters to minimize a non-linear function. It was necessary to implement this optimization routine, since my results were only numerical and would not provide any derivative information. I decided to optimize the sum of the squares of the relative errors between the predicted (Equations 1.15-1.17) and simulated fatigue behaviors.

The Nelder-Mead optimization is a simplex pattern search used to find a local minimum of a function of several variables using only function values, without any derivative information. For n variables, the simplex contains n+1 vertices. For our case the simplex is a tetrahedral. The method compares function values at the vertices of the simplex. Let $\Phi_k(\boldsymbol{x}_k)$ be the function that is to be minimized, where $\boldsymbol{x}_k = (K_n, K_D, K_{cr})$,

$$\Phi_k(\boldsymbol{x_k}) = \left[\left(\frac{(N_f)_{sim} - (N_f)_{pre}}{(N_f)_{pre}} \right)^2 + \left(\frac{\left(\frac{\Delta d}{\Delta n}\right)_{sim} - \left(\frac{\Delta d}{\Delta n}\right)_{pre}}{\left(\frac{\Delta d}{\Delta n}\right)_{pre}} \right)^2 + \left(\frac{\left(\frac{\Delta \varepsilon_{cr}}{\Delta n}\right)_{sim} - \left(\frac{\Delta \varepsilon_{cr}}{\Delta n}\right)_{pre}}{\left(\frac{\Delta \varepsilon_{cr}}{\Delta n}\right)_{pre}} \right)^2 \right]^{\frac{1}{2}} \quad (2.16)$$

The function value at the worst vertex is rejected and replaced with a new vertex. A new simplex is formed and the search is continued. The process generates a sequence of simplexes, for which the function values at the vertices get smaller and smaller. The sizes of the simplexes are reduced and the coordinates of the minimum point is found.

The simulated cycles to failure, $(N_f)_{sim}$ simulated damage rate, $(\Delta d/\Delta n)_{sim}$ and the simulated creep rate, $(\Delta \varepsilon_{cr}/\Delta n)_{sim}$ are calculated from the FE simulations as described above. The predicted cycles to failure, $(N_f)_{pre}$ predicted damage rate, $(\Delta d/\Delta n)_{pre}$ and the predicted creep rate, $(\Delta \varepsilon_{cr}/\Delta n)_{pre}$ are calculated using Equations 1.15-1.17.

The Nelder-Mead algorithm described below uses a set of constants in the calculation of various points throughout the algorithm, they are,

$$\rho = 1, \qquad \chi = 2, \qquad \gamma = \frac{1}{2}, \qquad \text{and } \sigma = \frac{1}{2}$$

To start, four vertices for the initial tetrahedral are chosen and the function values are computed and ranked from one to four, $\Phi(\boldsymbol{x}_1) \le \Phi(\boldsymbol{x}_2) \le \Phi(\boldsymbol{x}_3) \le \Phi(\boldsymbol{x}_4)$ one having the lowest value and four having the worst. Next the reflection point, $\boldsymbol{x}_r$ is calculated and evaluated,

$$\boldsymbol{x}_r = (1+\rho)\bar{\boldsymbol{x}} - \boldsymbol{x}_4 \quad (2.17)$$

where, $\bar{x} = \sum_{i=1}^{n} \frac{x_i}{n}$, is the centroid of the best points. If $\Phi_1 \le \Phi_r < \Phi_3$ then accept

reflection point $\boldsymbol{x}_r$ to replace $\boldsymbol{x}_4$ and move on to the next the iteration. If $\Phi_r < \Phi_1$ calculate and evaluate the expansion point $\boldsymbol{x}_e$,

$$\boldsymbol{x}_e = (1+\rho\chi)\bar{\boldsymbol{x}} - \rho\chi\boldsymbol{x}_4 \tag{2.18}$$

If $\Phi_e < \Phi_r$, accept $\boldsymbol{x}_e$ and stop the iteration, otherwise accept $\boldsymbol{x}_r$. If $\Phi_r \geq \Phi_3$ then a contraction must be performed. If $\Phi_3 \leq \Phi_r \leq \Phi_4$ then an outside contraction, $\boldsymbol{x}_{co}$ must be calculated and evaluated. If $\Phi_r \geq \Phi_4$ then perform an inside contraction, $\boldsymbol{x}_{ci}$ where.

$$\boldsymbol{x}_{co} = (1+\rho\gamma)\bar{\boldsymbol{x}} - \rho\gamma\boldsymbol{x}_4 \tag{2.19}$$

$$\boldsymbol{x}_{ci} = (1-\gamma)\bar{\boldsymbol{x}} + \gamma\boldsymbol{x}_4 \tag{2.20}$$

If the function value for the corresponding contraction is better than the reflection point, the contraction is accepted and the next iteration can started. If the function values of the corresponding contractions are worse than the reflection than a shrink must be performed. When performing the shrink a new simplex is formed by keeping $\boldsymbol{x}_1$ and replacing the other vertices with,

$$v_i = \mathbf{x}_1 + \sigma(\mathbf{x}_i - \mathbf{x}_1) \tag{2.21}$$

where i=2, 3, 4. Evaluate Φ at the new vertices of the simplex and order them as before, $\Phi_1 \leq \Phi_2 \leq \Phi_3 \leq \Phi_4$. Once the ordering is complete the next iteration can be started.

Chapter 3: Results

In this chapter, results from the FE simulations are presented. Section 3.1 describes the models generated and their properties. The optimization of the SMP1 (optimization) group is shown in section 3.2. The FEA Fatigue simulations and comparisons are shown in section 3.3.

3.1 Models Generated

Three models were created for each sample in the SMP1 group. All models were created with 8 node cube elements, where each node had three degrees of freedom. The models for the SMP1 group had element edge lengths of 0.28, 0.21 and 0.14 mm and were named “normal”, “fine” and “super fine” respectively. The number of nodes and elements for each model in the SMP1 (optimization) group are shown below in Table 3.1. Only a normal model for each sample in SMP2 (verification) group was produced. These model properties are shown in table 3.2. The normal, fine and super fine models for SMP1-5 is shown in Figure 3.1.

Table 3.1: Model properties for SMP1 group used for optimization of parameters

	Normal		Fine		Super Fine	
Model	elements	nodes	elements	nodes	elements	nodes
SMP1-1	4638	5855	10516	12549	35367	40004
SMP1-2	4575	5784	10757	12817	35340	40029
SMP1-3	4451	5607	10643	12720	35576	40223
SMP1-4	4726	5928	11075	13166	36109	40779
SMP1-5	4868	6111	10914	13060	35195	39905

Table 3.2: Model properties for SMP2 group used for verification

Model	elements	nodes
SMP2-1	4652	5836
SMP2-2	4167	5266
SMP2-3	4425	5619
SMP2-4	4889	6086
SMP2-5	5001	6284

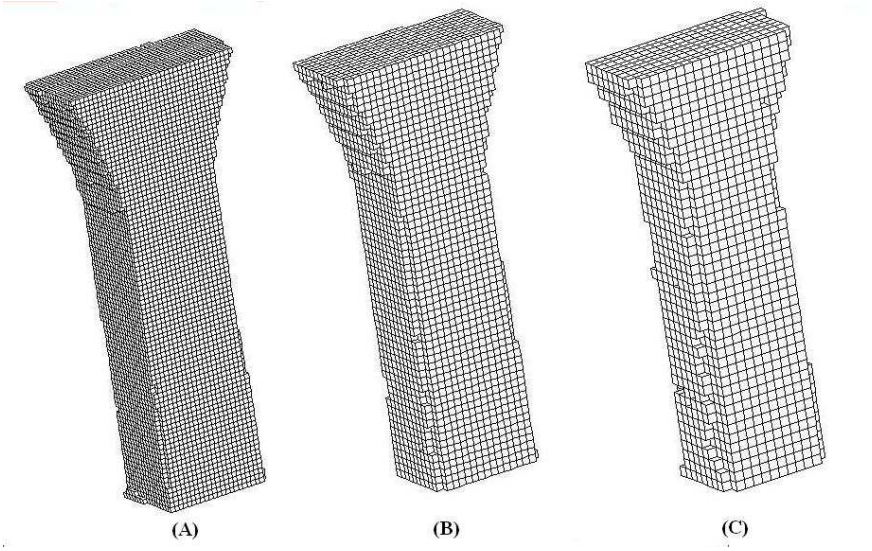

Figure 3.1: FE models for SMP1-5 showing effects of element sizes on surface geometry: (A) Super fine mesh with element edge length of 0.14 mm, (B) Fine mesh with element edge length of 0.21 mm, (C) Normal mesh with element edge length of 0.28 mm.

To demonstrate mesh convergence, moduli of all models in the SMP1 group are plotted against the number of elements (figure 3.2). It can be seen that the size of the element affects the model's modulus. The modulus increased as the mesh size decreased. All the moduli lay within the reported 14-20 GPa range for cortical bone (Taylor, O'Reilly et al. 2003). Figure 3.3 shows all the model's moduli for the SMP2 group.

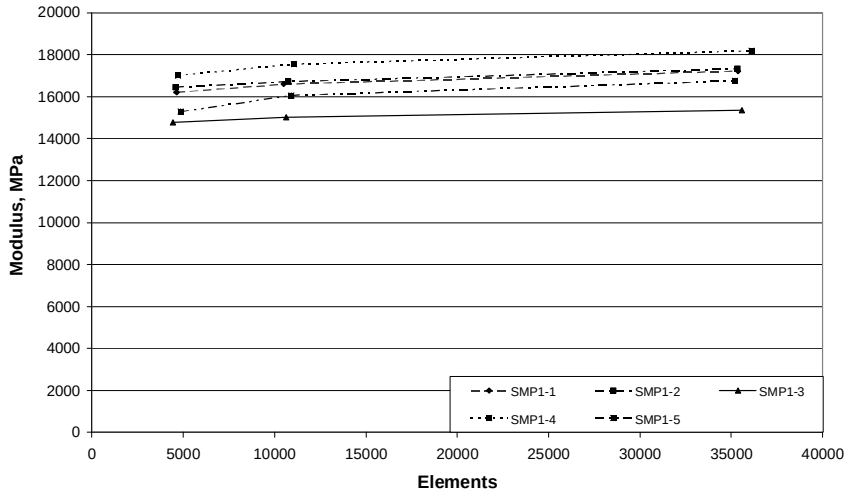

Figure 3.2: SMP1-normal model's moduli verse the number of elements in the mesh.

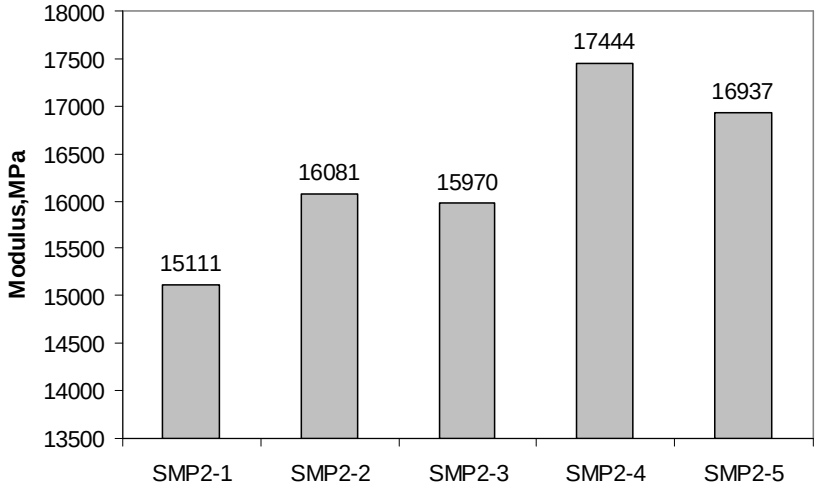

Figure 3.3: Sample modulus values for the SMP2 group models used for verification.

The inhomogeneity of typical samples can be seen in Figure 3.4; the SMP1 group normal mesh models are shown. Histograms of the SMP1group (Figure 3.5) show the distribution of the elements properties within the SMP1 group. All the models are quite

similar. This is not unexpected since all the samples were taken from the same donor. The inhomogeneity of the model was affected by the mesh size. Differences in material distributions when different meshes were used are shown in Figure 3.6.

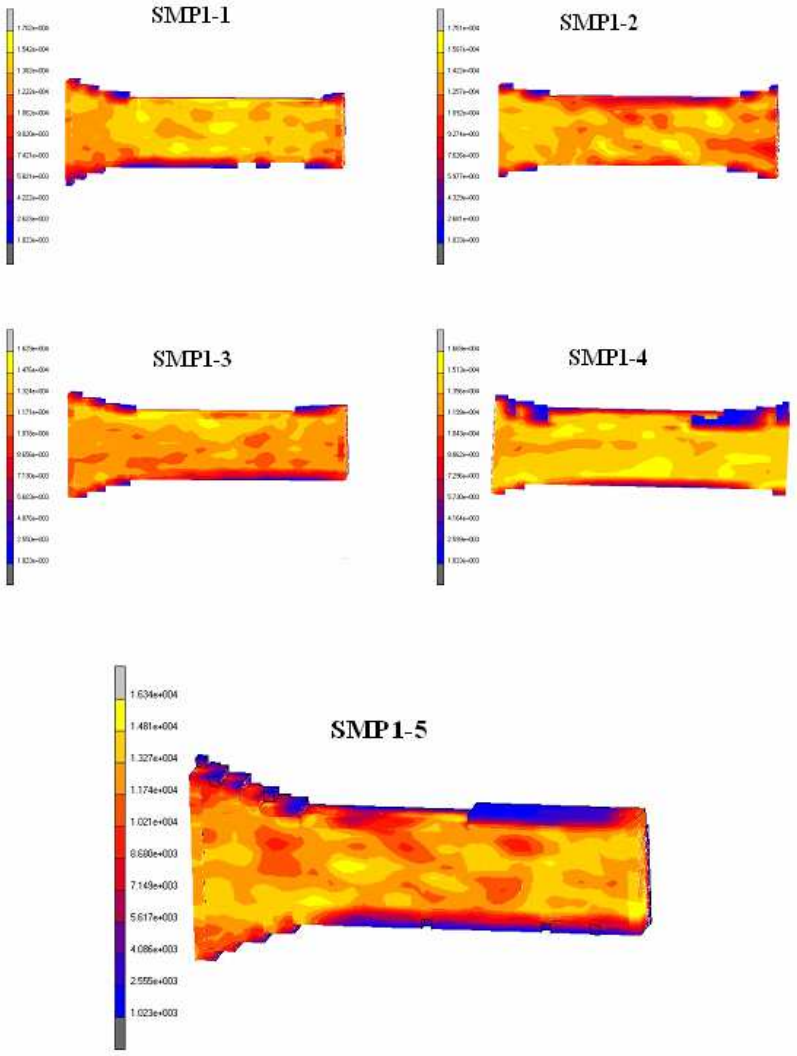

Figure 3.4: Non-homogeneous material distribution for SMP1 group.

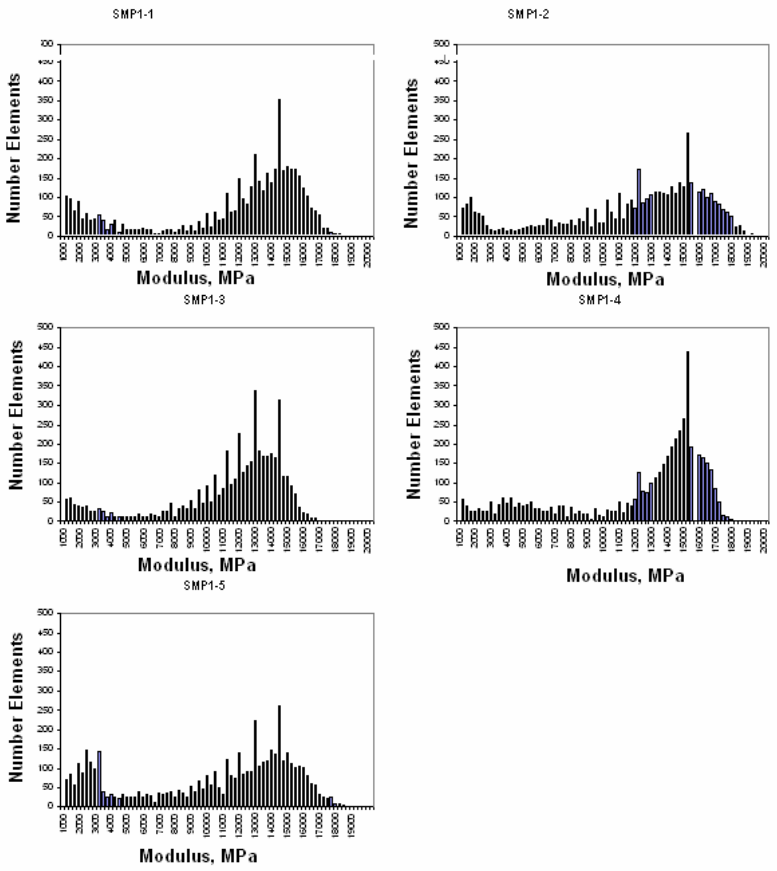

Figure 3.5: Element property distribution through SMP1group.

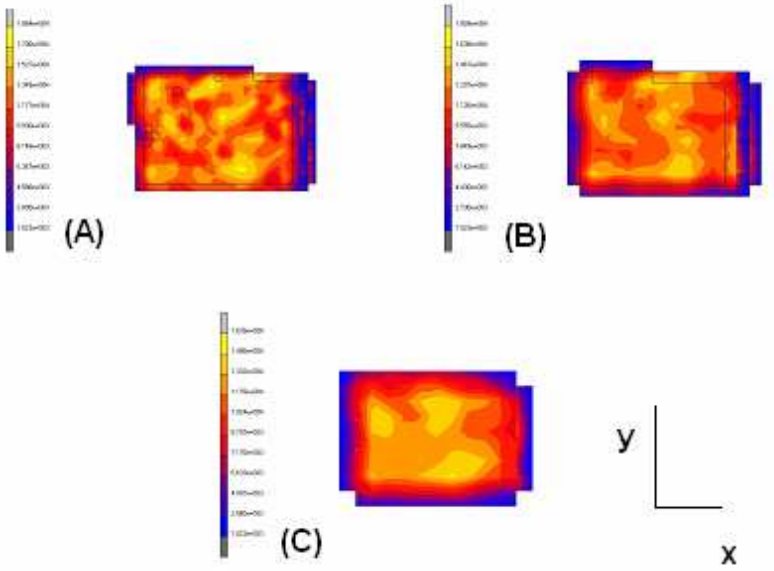

Figure 3.6: Cross section showing material property distribution at height z = 7.6 .mm for sample SMP1-5 ; (A) Super fine mesh, (B) Fine Mesh, (C) Normal Mesh

3.2 Nelder-Mead Optimization

The Nelder-Mead optimization was implemented to find the optimal K_N, K_D, and K_{cr} values for the normal samples in the SMP1 (optimization)group using Equation 2.16, the sum of the squares of the relative error of the fatigue behavior, where we were comparing the predicted (computed from Equations 1.15-1.17) and FEA simulated values. During the optimization and fatigue simulation the samples were loaded to fail around 1000 cycles. The load, predicted cycles to failure, predicted damage per cycle and predicted creep per cycle are shown below in Table 3.3. Figure 3.7 shows Φ verses the increment of the optimization for the SMP1 group as Φ converges towards zero. The values found for K_N, K_D, K_{cr} and Φ for the normal mesh models in SMP1 group are shown in Table 3.4.

Table 3.3: Forces and predicted fatigue behavior computed from Equations 1.15-1.17

Model	Force, N	N_F	Damage per cycle	creep per cycle
SMP1-1	420	1107	8.86E-05	1.35E-06
SMP1-2	420	1068	9.26E-05	1.41E-06
SMP1-3	385	1021	9.82E-05	1.49E-06
SMP1-4	445	982	1.03E-04	1.57E-06
SMP1-5	370	1008	9.98E-05	1.52E-06

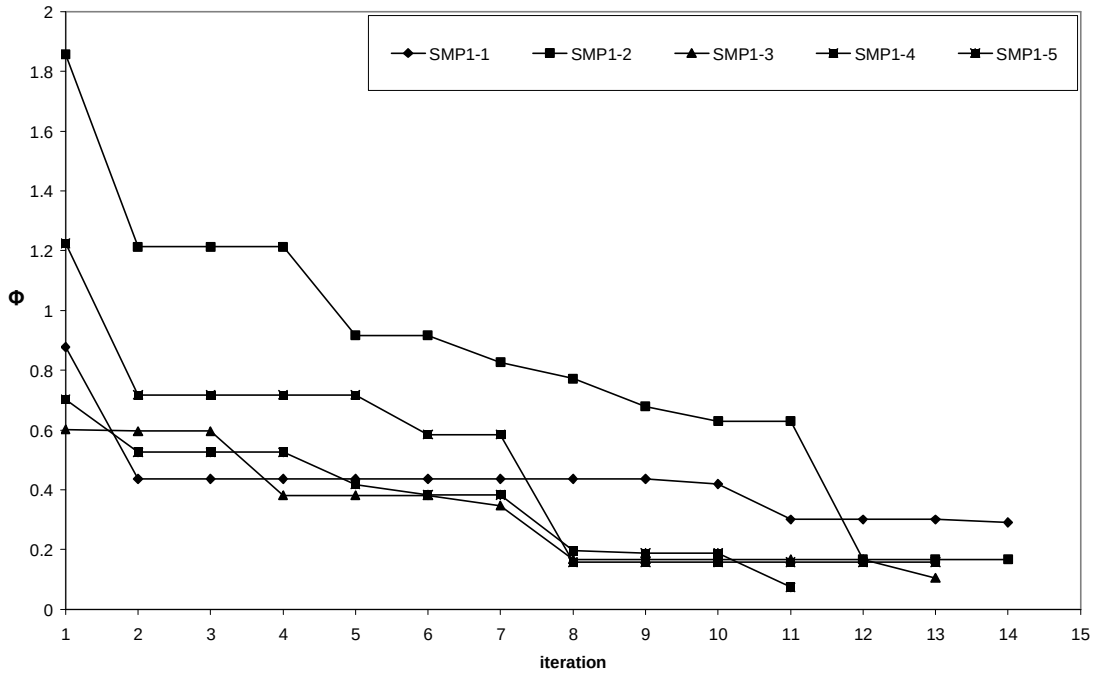

Figure 3.7: Φ vs. optimization iteration number for the SMP1 group normal mesh models, showing convergence

Table 3.4: Optimized sizing factors for the SMP1 Group

Model	K_N	K_D	K_{cr}	Φ
SMP1-1	1.12571916	1.0343457	1.02571	0.28
SMP1-2	1.17558585	1.0864702	1.03677	0.167
SMP1-3	1.08524502	1.0052714	0.99011	0.105
SMP1-4	1.1484225	1.0603338	1.02693	0.159
SMP1-5	1.07454347	0.9990848	0.98309	0.074

3.3 Fatigue Simulations

When the fatigue simulations were run for the normal mesh models in the SMP1 group without sizing factors, the cycles to failure were greatly under-predicted while the damage per cycle and creep per cycle were over-predicted. An example of this is

shown in Figure 3.8 for SMP1-5. In this FEA simulation the model failed at 100 cycles when it was loaded to fail at around 1000 cycles.

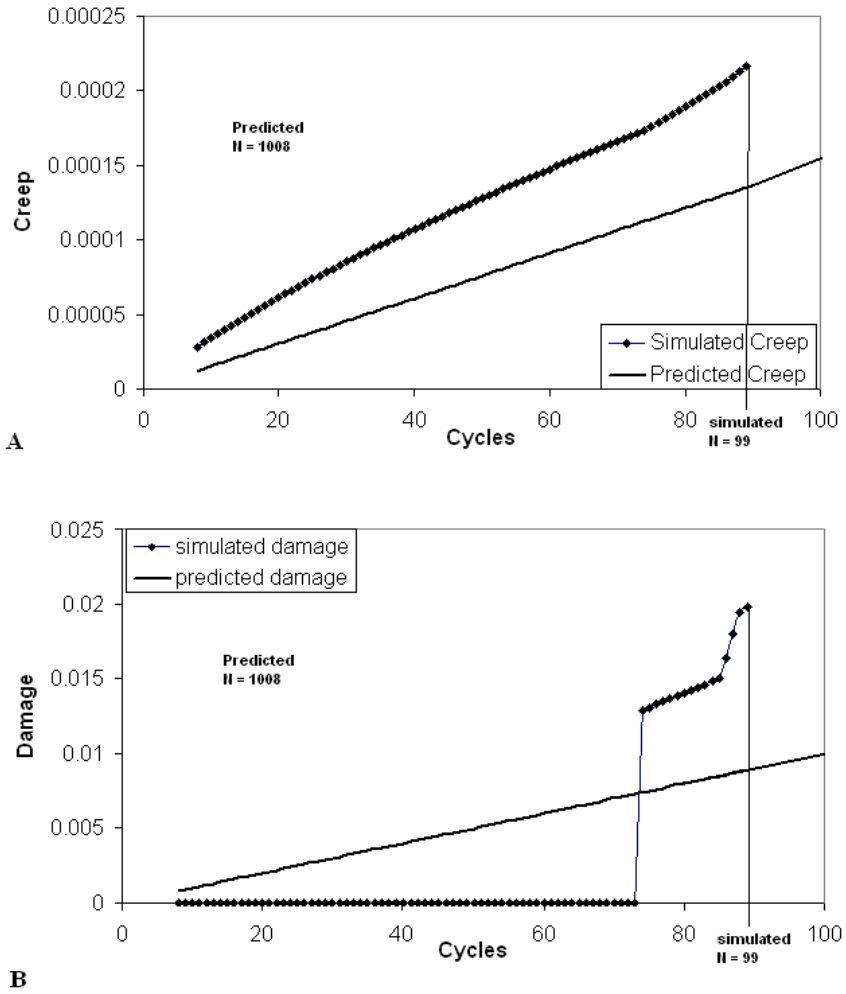

Figure 3.8: Comparison of predicted and simulated results. Predictions computed from Equations 1.16 and 1.17 and FEA simulation are results for SMP1-5 normal mesh without sizing factors. (A) Creep vs. number of cycles, (B) Damage vs. number of cycles. Model was loaded to fail around 1000 cycles but failed at 99 cycles.

Once the optimized sizing factors were applied to the simulations, the behavior was brought into closer agreement (Figure 3.9). A simulation was also run where only

the life sizing factor K_N was applied while the other sizing factors were not to see if it was necessary to include sizing factors on the damage and creep laws. This represents the current stressed volume approach, proposed for bone by Taylor, D. and Kuiper (2001). The cycles to failure (Figure 3.10), damage per cycle (Figure 3.11) and creep per cycle (Figure 3.12) for each simulation is shown below. The average percent error of the fatigue behavior is shown below (Table 3.5) for the simulations and was computed by taking an average of the sum of the simulated percent errors against the predicted fatigue behavior. The average for the group is also shown to try and display an overall trend. It is apparent that the simulations that included the optimized sizing factors greatly increased the accuracy of the simulations. The current stressed volume approach slightly improves the simulations.

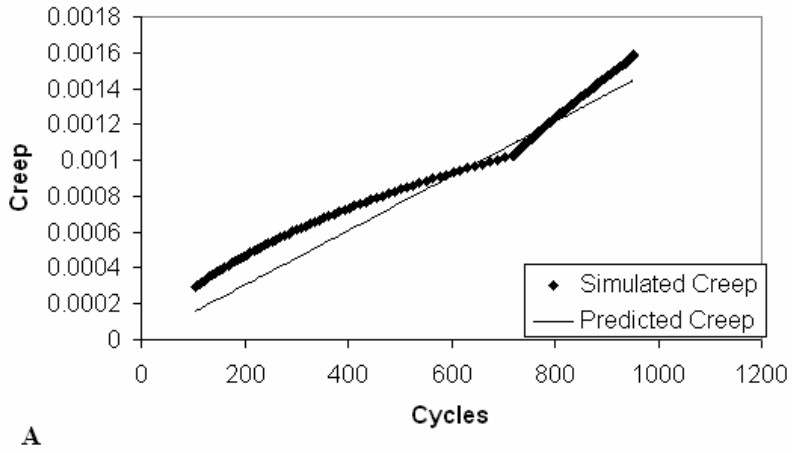

A

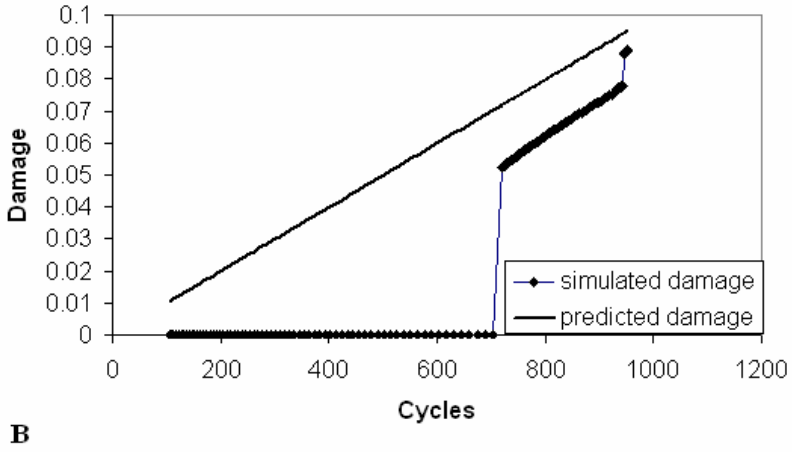

B

Figure 3.9: Comparison of predicted and simulated results. Predictions computed from Equations 1.16 and 1.17 and FEA simulation are results for SMP1-5 normal mesh using optimized sizing. (A) Creep vs. number of cycles, (B) Damage vs. number of cycles.

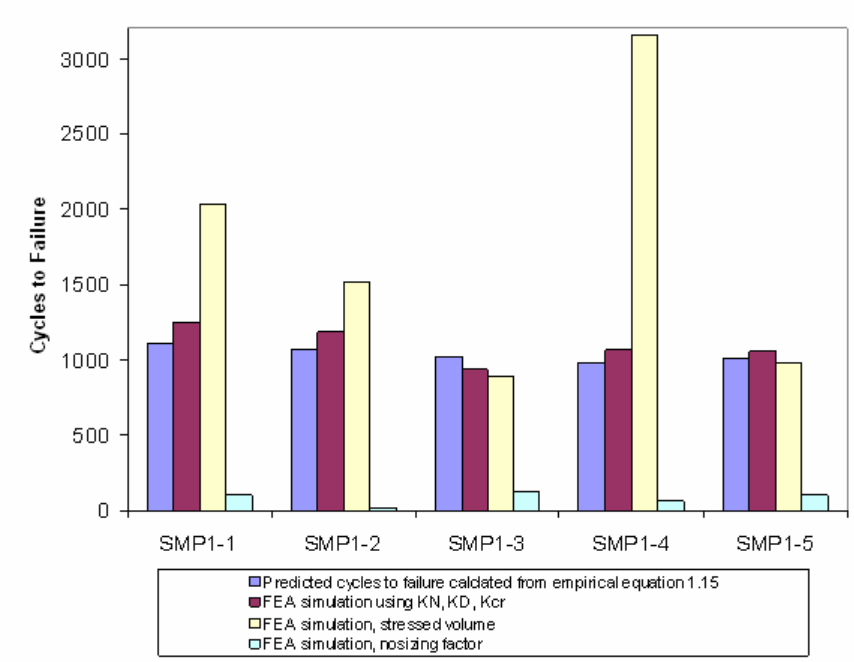

Figure 3.10: Cycles to failure comparisons; predicted value from empirical Equation 1.15, FEA simulation using optimized sizing factors K_N, K_D, K_{cr}, FEA simulation using only life sizing factor K_N, FEA simulation without any sizing factors.

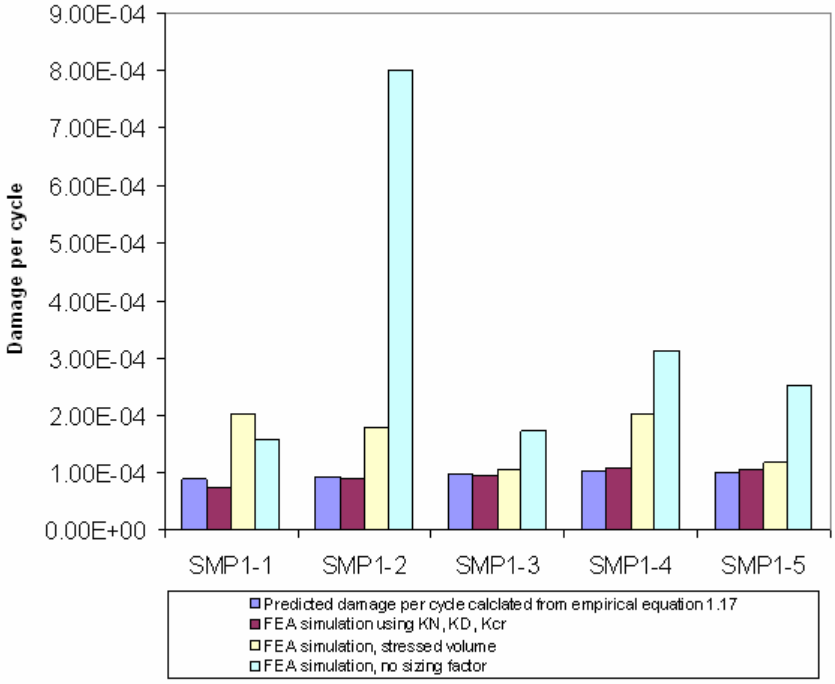

Figure 3.11: Damage per cycle comparisons; predicted value from empirical Equation 1.15, FEA simulation using optimized sizing factors K_N, K_D, K_{cr}, FEA simulation using only life sizing factor K_N, FEA simulation without any sizing factors.

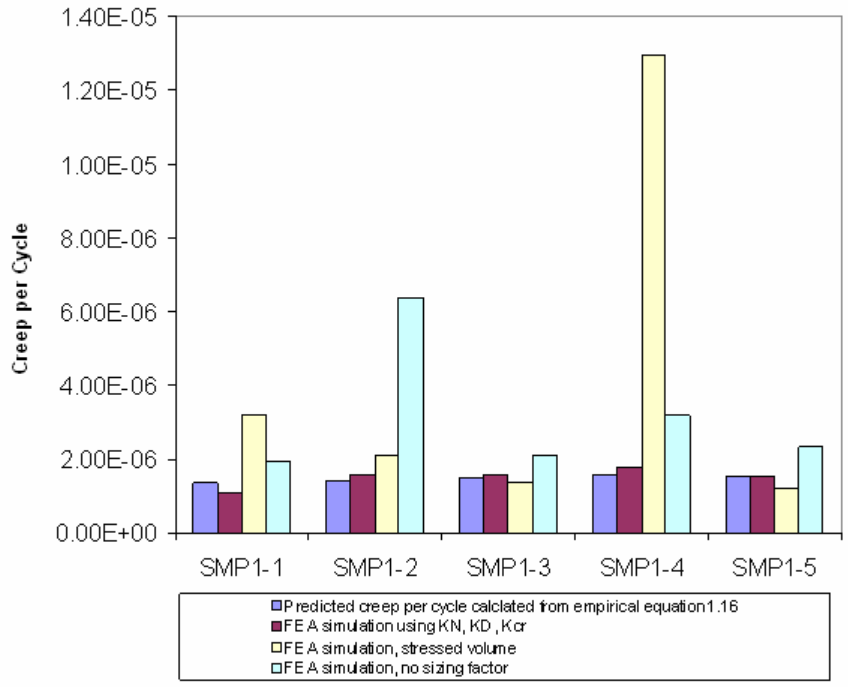

Figure 3.12: Creep per cycle comparisons; predicted value from empirical Equation 1.15, FEA simulation using optimized sizing factors K_N, K_D, K_{cr}, FEA simulation using only life sizing factor K_N, FEA simulation without any sizing factors.

Table 3.5: Average percent errors between FEA simulations and predictions for the SMP1 group

	K_N, K_D, K_{cr}	K_N only	No sizing factors
SMP1-1	15.95%	116.73%	70.26%
SMP1-2	9.14%	61.72%	405.57%
SMP1-3	5.71%	9.80%	67.98%
SMP1-4	8.67%	347.58%	132.55%
SMP1-5	3.53%	14.01%	97.79%
Average	8.60%	109.97%	154.83%

3.4 Validation of K_N, K_D, K_{cr}

To evaluate the success of the sizing factors found for the normal mesh models in the SMP1 group three sets of K_N, K_D, K_{cr} were run for the SMP2 group, a "low",

"mean" and a "high". The K_N values were used to choose the low and high values because most fatigue applications are life related. The mean was averaged from all values. The sizing factors, K_N, K_D and K_{cr} used for these evaluations are shown below in Table 3.6. A simulation was also run where no sizing factors were implemented to set a base for comparisons. The results from model SMP2-5 were excluded because it would break at the bottom of the sample after one cycle. This is similar to a sample breaking at the grips in a real test. The cycles to failure (Figure 3.13), damage per cycle (Figure 3.14) and creep per cycle (Figure 3.15) for each simulation is shown below. The average percent errors for the simulations are shown in Table 3.7. It can be seen that the high simulation improved the fatigue behavior the best.

Table 3.6: Sizing factors used to evaluate success on SMP2 verification models

Case	K_N	K_D	K_{cr}
K_{low}	1.074543	0.999085	0.983091
K_{mean}	1.121903	1.037101	1.012522
K_{high}	1.175586	1.08647	1.036767
No Sizing Factors	1	1	1

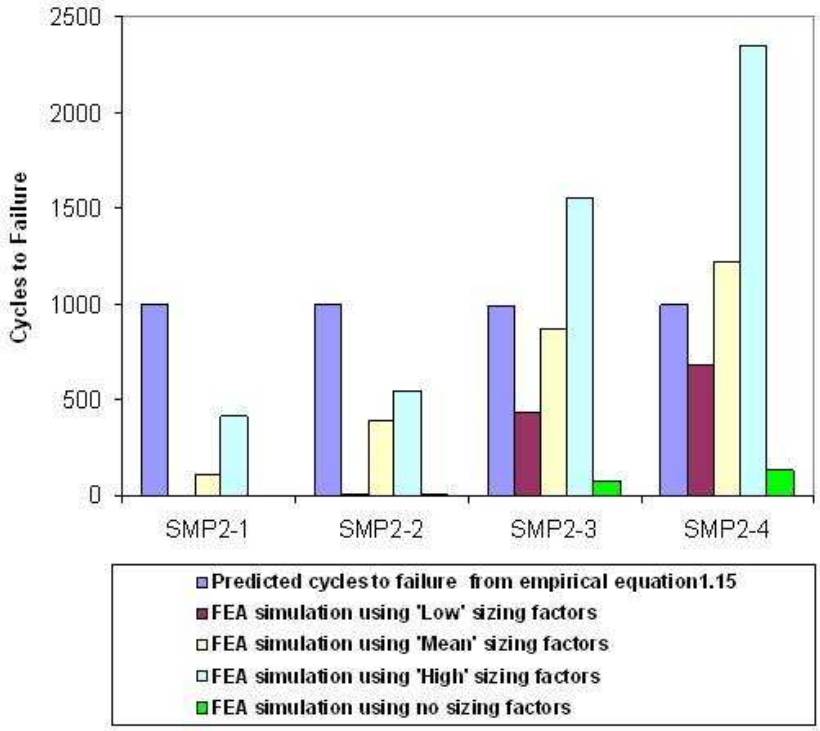

Figure 3.13: Comparison of cycles to failure for SMP2 group; predicted cycles to failure calculated from equation 1.15, FEA simulation using "low" sizing factors, FEA simulation using "mean" sizing factors, FEA simulation using "high" sizing factors, FEA simulation using no sizing factors.

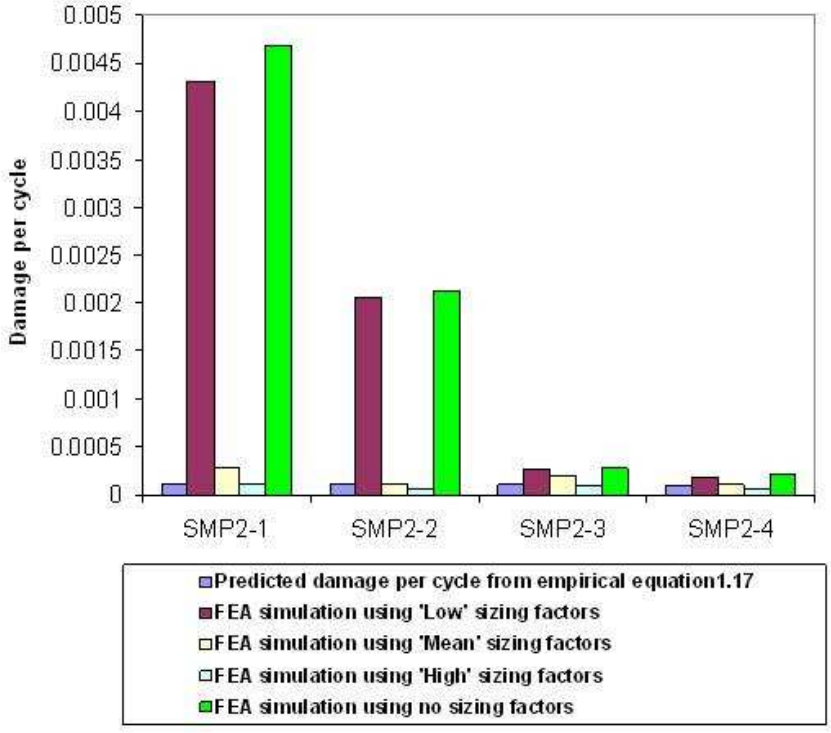

Figure 3.14: Comparison of damage per cycle for SMP2 group; predicted cycles to failure calculated from equation 1.15, FEA simulation using "low" sizing factors, FEA simulation using "mean" sizing factors, FEA simulation using "high" sizing factors, FEA simulation using no sizing factors.

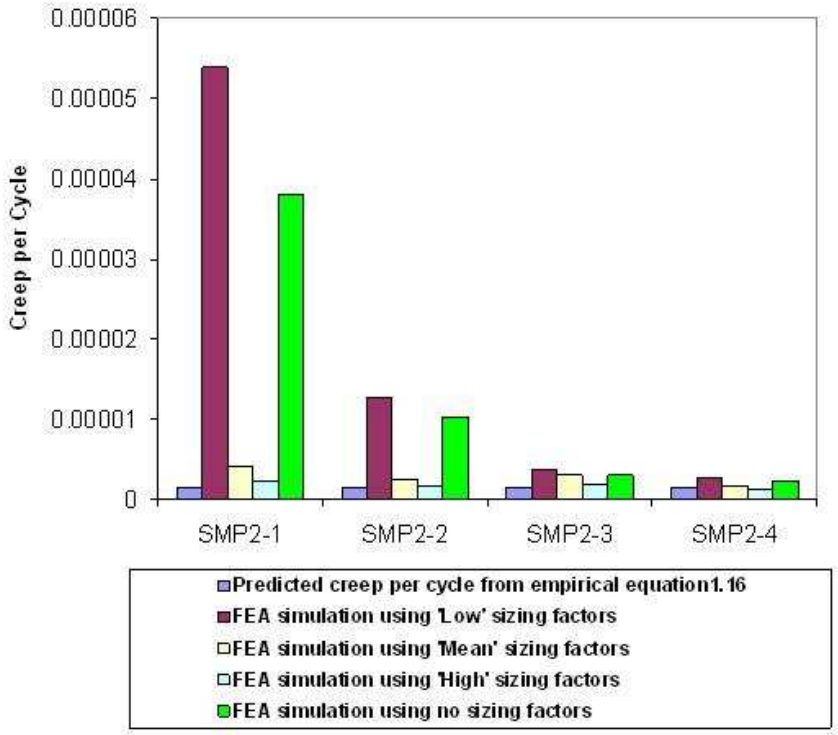

Figure 3.15: Comparison of creep per cycle for SMP2 group; predicted cycles to failure calculated from equation 1.15, FEA simulation using "low" sizing factors, FEA simulation using "mean" sizing factors, FEA simulation using "high" sizing factors, FEA simulation using no sizing factors.

Table 3.7: Average percent errors for SMP2 group

	K_{LOW}	K_{MEAN}	K_{HIGH}	No Sizing Factors
SMP2-1	2548.10%	145.53%	36.78%	2332.19%
SMP2-2	916.73%	40.73%	30.16%	891.48%
SMP2-3	116.38%	66.80%	27.92%	120.34%
SMP2-4	60.89%	15.37%	61.22%	82.05%
Average	910.52%	67.11%	39.02%	856.52%

Effects of Element Size on Sizing Factors.

To test the effect of mesh size on the sizing factors, model SMP1-5 using the fine mesh was run using the sizing factors optimized from the SMP1-5 normal mesh. Using the sizing factors from the normal mesh on the fine mesh gave an average percent error of 73.69 % from the predicted behaviors. An optimization was performed on the fine mesh (figure 3.16) to compare the sizing factors computed, the values are shown in Table 3.8. Running the fine model with sizing factors from the normal model improved the behavior (Figures 3.17, 3.18 and 3.19) but the optimized results for the fine model produced improved averaged behavior by 56% over the sizing factors optimized from normal mesh.

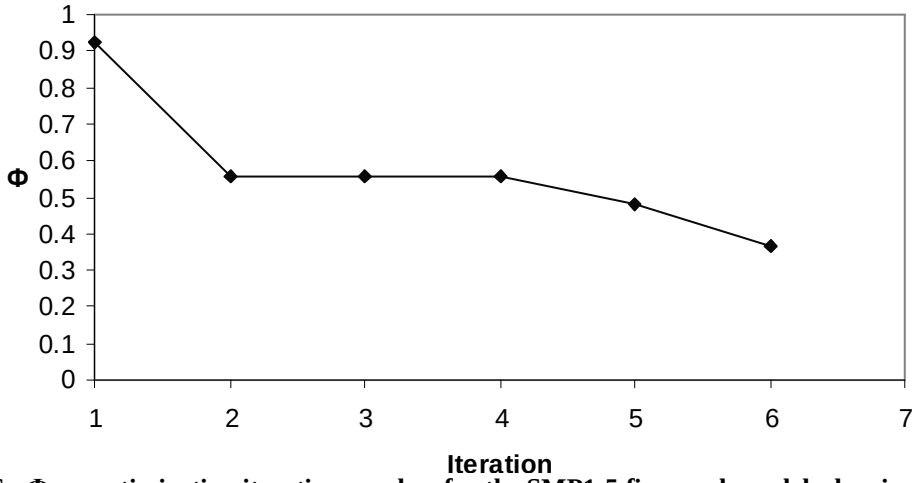

Figure 3.16: Φ vs. optimization iteration number for the SMP1-5 fine mesh model, showing convergence

Table 3.8: Sizing factors and average percent errors for SMP1-5 fine mesh

Simulation	K_N	K_D	K_{cr}	Average errors
No Sizing	1	1	1	107.22%
Normal Optimized	1.074543	0.999085	0.983091	73.69%
Fine Optimized	1.132407	1.056481	1.007407	17.39%

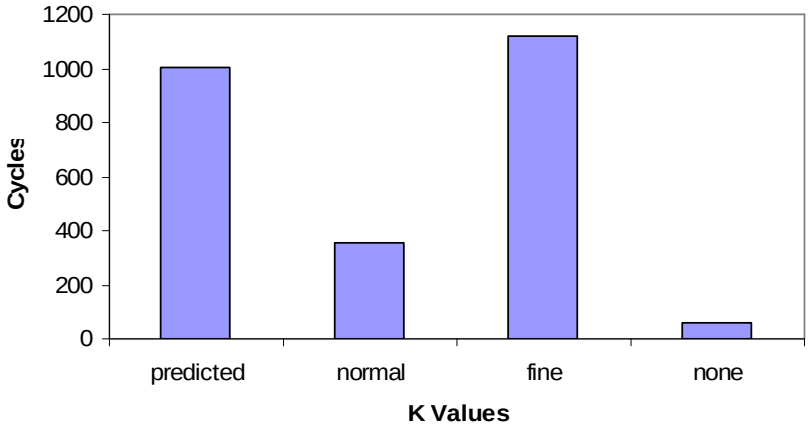

Figure 3.17: Comparison of cycles to failure for the SMP1-5 fine mesh: Predicted cycles to failure from Equation 1.15, FEA simulation using sizing factors optimized from the normal mesh, FEA simulation using sizing factors optimized from the fine mesh, FEA simulation using no sizing factors.

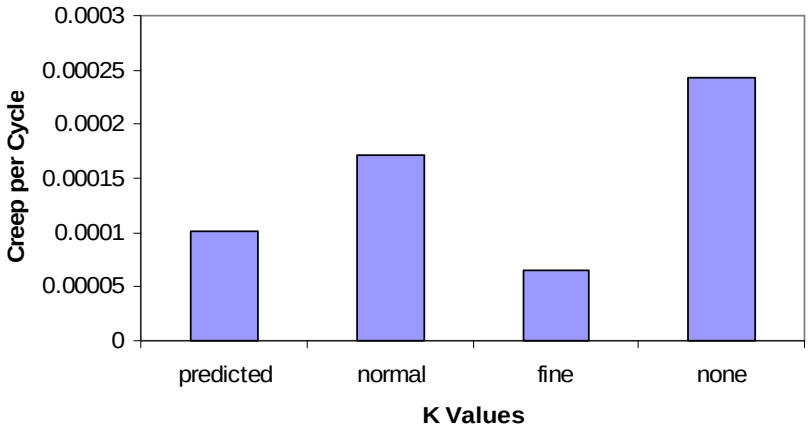

Figure 3.18 : Comparison of creep per cycle for the SMP1-5 fine mesh: Predicted cycles to failure from Equation 1.16, FEA simulation using sizing factors optimized from the normal mesh, FEA simulation using sizing factors optimized from the fine mesh, FEA simulation using no sizing factors.

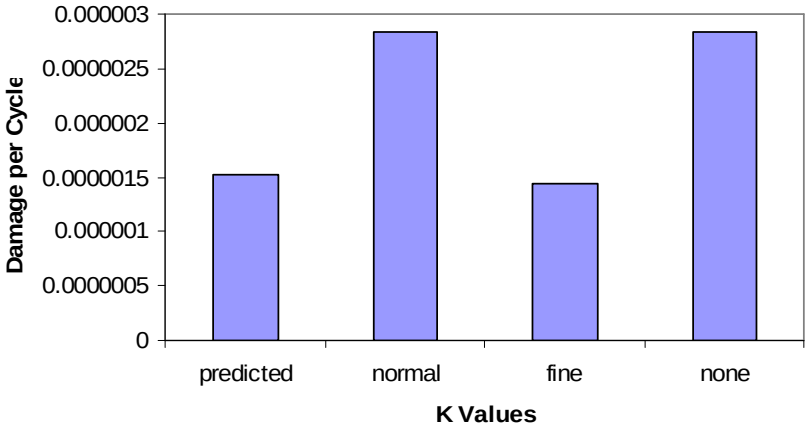

Figure 3.19 : Comparison of damage per cycle for the SMP1-5 fine mesh: Predicted cycles to failure from Equation 1.17, FEA simulation using sizing factors optimized from the normal mesh, FEA simulation using sizing factors optimized from the fine mesh, FEA simulation using no sizing factors.

Chapter 4: Discussion

This chapter discusses the outcomes of the fatigue simulations. The significance of automatic meshing is observed in Section 4.1. Element size is discussed in Section 4.2, showing the importance of these properties. The damage accumulation is discussed in section 4.3. Section 4.4 discusses the effectiveness of the sizing factors. Finally, a summary of the important conclusions is given in Section 4.5.

4.1 Automatic meshing

CT images provide an excellent source for model geometry and material properties for bone. The images I used were micro CT images with a resolution of 14.95 µm. The resolutions of normal scanners do not capture this fine of a detail. The automated voxel meshing technique provided an easy method of generating meshes of our samples quickly. The technique has been criticized (Viceconti, Bellingeri et al. 1998) because it does not accurately model curved surface geometries due to the use of regular 8–noded cube elements. This was not a major concern of ours because the surfaces of our samples were mostly flat. Further, because our samples were loaded in uniaxial tension, we do not get the high surface stresses as seen in bending. It was shown in Figure 3.1 that while the element size did affect the surface geometry slightly, this did not effect my simulations as I could see with the slight variation in sample modulus. Alternative techniques of solid modeling followed by automated 3D meshing are time consuming and would have added months to the project to create all the FE meshes used.

The computed model modulus lay within the reported 14-20 GPa range for cortical bone (Taylor, O'Reilly et al. 2003).

4.2 Element size effects

It was shown (Figure 3.2) that as the element size decreased the model stiffness increased. Usually in finite element models the stiffness is over predicted by a coarse mesh. The reason for our results are that the edge elements are softer in the more coarse meshes, because when the super voxels near the edges are being created by averaging in more voxels with lower CT numbers are include and averaged. This can be seen in Figure 4.1; where the blue represents a lower modulus, C represents the normal mesh; B represents the fine mesh, and A shows the super fine mesh. The amount of weaker elements decreases as the mesh size is refined. Furthermore the relationship between voxel brightness and modulus is nonlinear. I saw slight variations in modulus, however due to simulation time constraints, I concentrated on the normal mesh size.

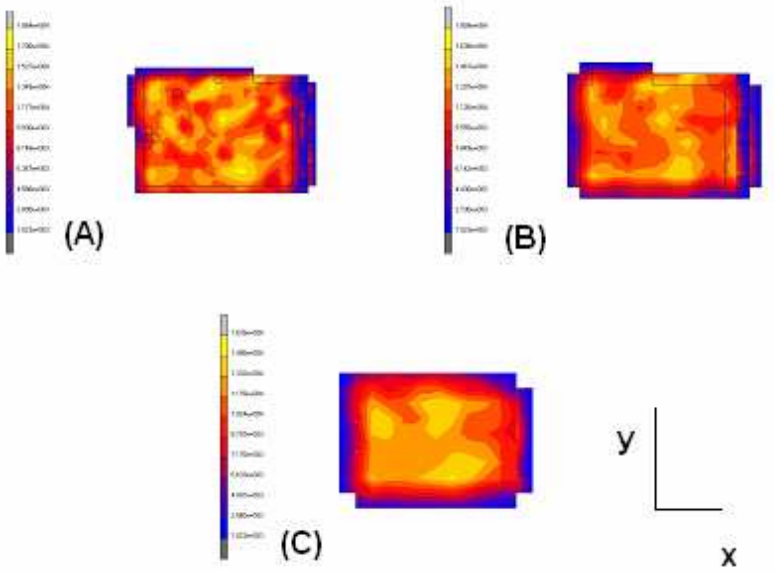

Figure 4.1: Cross section showing material property distribution at z = 7.6 .mm for SMP1-5; (A) Super fine mesh, (B) Fine Mesh, (C) Normal mesh

4.3 Damage in the Finite Element Simulations

During the FEA simulations I noticed that some of the models initially experienced little or zero damage and then the damage would experience a huge increase (Figure 3.8 (B) and3.9 (B)). In real tests the damage accumulates more gradually. One possible cause fore this jump could be the use of the coarse mesh. As one element fails there is a large reduction in the surface area

The use of clinical scanners would cause the use of coarse meshes due to the fact that they are unable to produce scans with such a fine resolution as I used. I think that this further work must be performed to explain the sudden jumps in the damage seen in some of the simulations.

4.4 Sizing Factors Effectiveness

I was able to show that by applying the sizing factors to the damage laws within the fatigue simulation, I was able to improve the accuracy of the simulated behavior. By using a numerical optimization I was able to find a set of sizing factors for each individual model in the SMP1 optimization group normal mesh. The average percent error for the group was 9%; while the current stressed volume approach yielded an average error of 110%

When the optimized sizing factors were tested for effectiveness on other models in the SMP2 or verification group, the high and mean simulations improved the behaviors, with average percent errors of 39% and 67% respectively. The errors in the SMP2 group were overall higher than in the optimized group but they still showed improved simulated behavior over the previous methods where no sizing factors, or sizing factor applied only to the life law were used.

The optimal sizing factor for the SMP1-5 normal mesh was tested on the SMP1-5 fine mesh model to check the effects of the mesh size on the sizing factors. Applying the normal sizing factors to the SMP1-5 fine mesh model improved the behavior and gave an average percent error of 74%. Running the optimization to find the better sizing factors for the fine mesh gave: K_N =1.132407, K_D =1.056481 and K_{cr} =1.007407. All these values are greater than the normal sizing factors found for SMP1-5. Running the simulation with the new sizing factors gave an average percent error of 17%. This shows that the size of the mesh affects the sizing factors for a model.

4.5 Summary

The novel approach of this thesis applies sizing factors to creep, damage and life laws within fatigue simulations. The automatic voxel meshing technique allowed us to easily produce non-homogeneous FE models using micro CT images as source information for geometry and material properties. I showed that applying these sizing factors to simulations of non-homogeneous FE models improved the accuracy of the simulation. I also showed that the use of all three sizing factors is more effective than just using the life sizing factor of the current stressed volume approach (Taylor and Lee 2003). I used Nelder-Mead optimization to find optimal sizing factor for individual models. I showed that these optimized values could be used on other models, still improving the simulations. Finally, I showed it was more effective to perform a new optimization for different models and mesh sizes.

Chapter 5: References

Basquin, O. H. (1910). "The Exponential Law of Endurance Tests." Am. Soc. Test. Mater **Proc., 10**: 625-630.

Carter, D. R. and W. E. Caler (1983). "Cycle-dependent and time-dependent bone fracture with repeated loading." Journal of Biomechanical Engineering **105**: 166-170.

Carter, D. R. and W. C. Hayes (1977). "The compressive behavior of bone as a two-phase porous structure." Journal of Bone Joint Surgery **59A**: 954-962.

Cotton, J., K. Winwood, et al. (2005). "Damage Rate is a Predictor of Fatigue Life and Creep Strain Rate in Tensile Fatigue of Human Cortical Bone Samples." Journal of Biomechanical Engineering **127**: 213-219.

Cotton, J. R., P. Zioupos, et al. (2003). "Analysis of creep strain during tensile fatigue of cortical bone." Journal of Biomechanics **36**(7): 943-949.

Courtney, A. C., W. C. Hayes, et al. (1996). "Age related differences in post-yield damage in human cortical bone, experiment and model." Journal of Biomechanics **29**: 1463.

Cowin, S. C., Ed. (2001). BoneMechanichs handbook. Boca Raton, FL, CRC Press.

Donahue, S. W., N. A. Sharkey, et al. (2000). "Bone Strain and Microcracks at Stress Fracture Sites in Human Metatarsals." Bone **27**(6): 827-833.

Goodenough, D. J. (2000). Tomographic Imaging. Bellingham, SPIE Press,**:** 511-54.

Kachanov, L. M. (1986). Introduction to Continuum Damage Mechanics. Dordrecht, netherlands.

Keyak, J. H., M. G. Fourkas, et al. (1993). "Validation of an automated method of three dimensional finite element modelling of bone." Journal of Biomechanical Engineering **15**: 505-509.

Keyak, J. H., J. M. Meagher, et al. (1990). "Automated three-dimensional finite element modeling of bone: a new method." Journal of Biomechanical Engineering **12**: 389-397.

Keyak, J. H., S. A. Rossi, et al. (2001). "Prediction of fracture location in the proximal femur using finite element models." Mechanical Engineering & Physics **23**(657-664).

Lee, T. C., F. J. O'Brien, et al. (2000). "The nature of fatigue damage in bone." International Journal of Fatigue **22**(10): 847-853.

McBroom, R. J., W. C. Hayes, et al. (1985). "Prediction of vetebral body compression fracture using quantitative computed tomography." Journal of Bone Joint Surgery **67A**: 1206-1214.

Pattin, C. A., W. E. Caler, et al. (1996). "Cyclic mechanical property degradation during fatigue loading of cortical bone." Journal of Biomechanics **29**(1): 69-79.

Taddei, F., A. Pancanti, et al. (2004). "An improved method for the automatic mapping of computed tomography numbers onto finite element models." Medical Engineering & Physics **26**(1): 61-69.

Taylor, D. and J.-H. Kuiper (2001). "The prediction of stress fractures using a 'stressed volume' concept." Journal of Orthopaedic Research **19**(5): 919-926.

Taylor, D. and T. C. Lee (2003). "A crack growth model for the simulation of fatigue in bone." International Journal of Fatigue **25**(5): 387-395.

Taylor, D., P. O'Reilly, et al. (2003). "The fatigue strength of compact bone in torsion." Journal of Biomechanics **36**(8): 1103-1109.

Taylor, M., J. Cotton, et al. (2002). "Finite Element Simulation of the Fatigue Behaviour of Cancellous Bone." Meccanica **37**(4 - 5): 419-429.

Taylor, M. and E. Tanner (1997). "Fatigue failure of cancellous bone: a possible cause of implant migration and loosening " The Journal of Bone and Joint Surgery British Volume **79-B**: 181-182.

Taylor, M., N. Verdonschot, et al. (1999). "A combined finite element method and continuum damage mechanics approach to simulate the in vitro fatigue behavior of human cortical bone." Journal of Material Science: Materials in Medicine **10**: 841-846.

Valimaki, V.-V., H. Alfthan, et al. (2005). "Risk factors for clinical stress fractures in male military recruits: A prospective cohort study." Bone **37**(2): 267-273.

Viceconti, M., L. Bellingeri, et al. (1998). "A comparative study on different methods of automatic mesh generation of human femurs." Medical Engineering & Physics **20**(1): 1-10.

Zioupos, P., J. D. Currey, et al. (2001). "Tensile Fatigue in Bone: Are Cycles-, or Time to Failure, or Both, Important?" Journal of Theoretical Biology **210**(3): 389-399.

Zioupos, P., J. D. Currey, et al. (1994). "An examination of the micromechanics of failure of bone and antler by acoustic amission tests and Laser Scanning Confocal Microscopy." Medical Engineering & Physics **16**: 203.

Zioupos, P., X. Wang, et al. (1996). "The accumulation of fatigue microdamage in human cortical bone of two different ages in vitro." Clinical Biomechanics **11**(7): 365-375.

Zioupos, P., X. T. Wang, et al. (1996). "Experimental and theoretical quantification of the development of damage in fatigue tests of bone and antler." Journal of Biomechanics **29**(8): 989-1002.